

IsoDAR@Yemilab: Preliminary Design Report - Volume I: Cyclotron Driver

Abstract: This Preliminary Design Report (PDR) describes the IsoDAR electron-antineutrino source. Volumes I and II are site-independent and describe the cyclotron driver providing a 10 mA proton beam, and the medium energy beam transport line and target, respectively. Volume III describes the installation at the Yemilab underground laboratory in South Korea. The IsoDAR driver and target will produce a mole of electron-antineutrinos over the course of five years. Paired with a kton-scale liquid scintillator detector, it will enable an impressive particle physics program including searches for new symmetries, new interactions and new particles. Here in Volume I, we describe the driver, which includes the ion source, low energy beam transport, and cyclotron. The latter features radiofrequency quadrupole (RFQ) direct axial injection and represents the first accelerator purpose-built to make use of vortex motion.

Section Editors: M. Abs¹, J.R. Alonso², J.M. Conrad², M. Abs¹, E. Forton¹, D. Joassin¹, J. Moon², S. de Neuter¹, E. Van der Kraaij¹, G. Wéry¹, D. Winklehner²

for the IsoDAR collaboration

¹Ion Beam Applications, 3 chemin du cyclotron Louvain-la-Neuve, BELGIUM

²Massachusetts Institute of Technology, 77 Massachusetts Ave. Cambridge, MA, USA

Corresponding Authors: Joshua Spitz (spitzj@umich.edu) and Daniel Winklehner (winklehn@mit.edu)

V0.9

Contents

1	Introduction	5
1.1	The IsoDAR Physics Case	7
1.1.1	Fluxes in IsoDAR	7
1.1.2	New Particles: Experimentally and Theoretically Motivated	8
1.1.3	New Symmetries: Strong CP Violation and the QCD Axion	9
1.1.4	New Interactions: Tests via Precision Electroweak Physics	10
1.2	Requirements for the Proton Driver	11
2	Design of the Front End	12
2.1	The Ion Source	12
2.1.1	Design	12
2.1.1.1	Gas Input	12
2.1.1.2	Ionization by the Filament	12
2.1.1.3	Confinement & Extraction of the Plasma	13
2.1.2	Performance	14
2.1.2.1	Goals & Measurement Methods	14
2.1.2.2	Optimization of Ion Source Parameters	15
2.1.2.3	Latest Optimized Results	16
2.2	The Low Energy Beam Transport	17
2.2.1	Design Overview	17

2.2.2	Beam Steering & Chopping	17
2.2.3	Beam Dynamics	18
2.3	The Radiofrequency Quadrupole	19
2.3.1	Technical Design	21
2.3.2	Beam Dynamics	21
3	Design of the Cyclotron	23
3.1	Magnet Yoke	23
3.1.1	Design and fabrication of the cyclotron magnet	24
3.2	Interface with the RFQ	26
3.3	Central Region	29
3.3.0.1	Spiral Inflector Design	29
3.4	Vacuum Chamber	32
3.5	Coil configuration	33
3.6	Cyclotron RF System	34
3.7	RF Cavities (Dees, Stems and Liners)	35
3.7.1	Integration of preliminary central region in RF Cavities	35
3.7.2	RFQ Integration in RF Cavities	36
3.7.3	RFQ getter pumps in RF Cavities	37
3.7.4	RF Cavities design optimization	38
3.7.4.1	Performance requirement target	38
3.7.4.2	Parametric optimization of the design	38
3.7.5	RF cavity computation results	39
3.7.5.1	Detailed power analysis	41

3.7.5.2	Radial voltage dependency	43
3.7.6	RF Tuning System	44
3.7.7	RF Amplifiers	44
3.7.8	RF Lines and Couplers	45
3.7.9	LLRF Electronics	47
3.8	Cyclotron magnetic performance	49
3.8.1	Isochronization	49
4	Installation in the Yemilab Setting	51
4.1	Transport of Components	52
4.2	Assembly underground	54
5	Conclusion	57
5.1	Summary	57
5.2	Acknowledgements	57

Chapter 1

Introduction

IsoDAR will be the first high-intensity, proton-driven source to be located alongside an underground multi-kiloton-scale scintillator detector. The first version of IsoDAR will be constructed at the Yemilab facility [2] within the Handuk mine, located in South Korea where the “Liquid Scintillator Counter” (LSC) is planned to be installed [3]. The novel source, consisting of a cyclotron, beam transport line, and a target/sleeve is shown in Fig. 1.1. In five calendar years (four live years), the source will produce 1.67 million $\bar{\nu}_e + p \rightarrow e^+ + n$ (inverse beta decay or “IBD”) events and 7000 $\bar{\nu}_e + e^- \rightarrow \bar{\nu}_e + e^-$ (elastic scattering or ES) events in the LSC that can be used for searches for new physics. More than a mole of neutrons and monoenergetic photons are also produced in the target, and these may act as progenitors for new particles that enter the LSC and leave signatures from interactions and decays. IsoDAR can address a broad range of new physics manifested as new symmetries, new interactions and new particles that is inaccessible to traditional experiments. For further discussion see Refs. [4], [5].

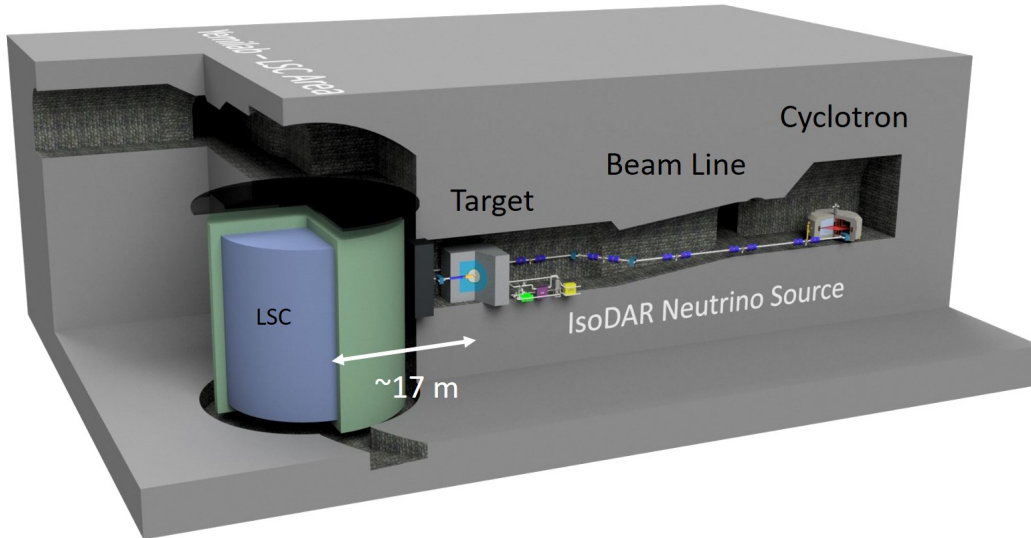


Figure 1.1: Schematic of the IsoDAR experiment installed at the Yemilab facility in South Korea. From right to left: The compact cyclotron with RFQ injector, the medium energy beam transport, the target, and the LSC neutrino detector. From [1].

This document is Volume 1 in a three-volume Preliminary Design Report (PDR) for IsoDAR that provides the engineering solutions necessary to establish credible solutions to the key issues and cost-drivers identified during the past decade of conceptual design and R&D. The contents of the PDR will cover the Technical Facility: the cyclotron, the beam transport and the target/sleeve. This document builds on the structure and text of the Conceptual Design Report (CDR) of the IsoDAR Technical Facility [6]. This step of producing a PDR substantially reduces risk related to IsoDAR approval: the remaining detailed engineering that will follow will build on these results and be straightforward to estimate in scope and cost.

Volume 1 describes the IsoDAR proton driver. This consists of a “front end” that delivers ions to a cyclotron for acceleration and extraction and the cyclotron itself. This document presupposes a basic understanding of cyclotrons; for an introduction to cyclotrons and a cost/benefit analysis of this choice of machine for IsoDAR, see the discussion in the CDR.

The 60 MeV/amu IsoDAR Proton Driver is exceptional in that it is designed and engineered to produce an order of magnitude higher intensity proton beam at extraction than commercial machines of similar energy. Achieving this high power necessitated three key breakthroughs. First, the cyclotron accelerates H_2^+ , mitigating “space charge effects” (electromagnetic interactions between beam particles). Second, the beam is axially injected through an RFQ, acting as a high-efficiency buncher. Third, the design harnesses vortex motion, a complex effect previously observed at PSI Injector II [7], [8], inducing stable spiraling motion in the high-current accelerated beam, significantly reducing beam growth. For more concerning the accelerator physics that shapes the IsoDAR design, see Ref. [9], [10].

These three physics requirements for reaching high current drive many of the engineering choices presented in this PDR. The other design driver is the need to construct the cyclotron underground. The cavern for the IsoDAR Proton Driver has already been constructed at Yemilab, and so the dimensions and constraints are understood, leading to fully realistic engineering plans.

This PDR is structured as follows:

Chapter 1: (This chapter) proceeds with an overview of the physics searches that will be possible with IsoDAR, followed by an overview of the requirements for the proton driver.

Chapter 2: Describes engineering related to the IsoDAR front end.

Chapter 3: Describes engineering related to the general IsoDAR cyclotron design.

Chapter 4: Describes specifics of the design related to installation underground.

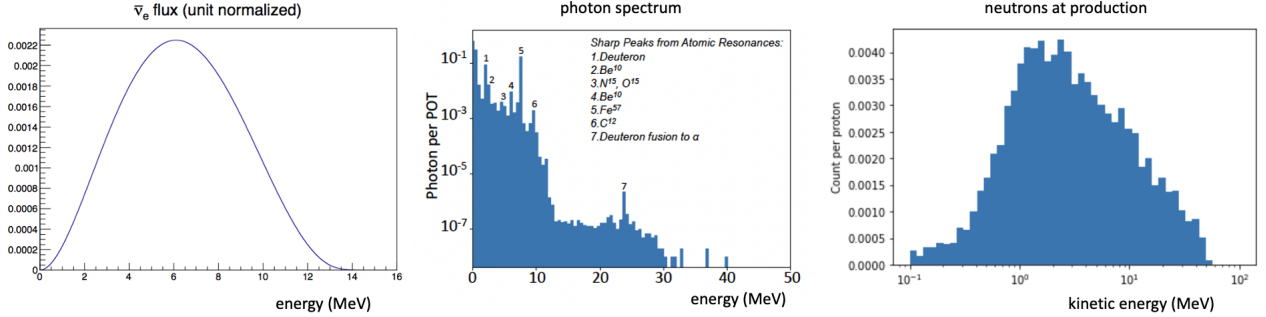


Figure 1.2: *Energy dependence of fluxes. Left: $\bar{\nu}_e$, unit normalized; Middle: photons per proton on target (POT) from excited nuclei. Right: kinetic energy of neutrons at production in target and sleeve, normalized per proton.*

1.1 The IsoDAR Physics Case

IsoDAR offers a rich BSM physics program if paired with a kton-scale liquid scintillator detector like the proposed LSC at Yemilab [3]. The exceptional reach is owed to the high flux rates of $\bar{\nu}_e$, photons, and neutrons from the $\approx 2 \cdot 10^{24}$ protons on target over 5 years (cf. Fig. 1.2), and placing the source very close to the detector. Here we briefly discuss the highlights of the IsoDAR BSM physics program enabled by a 2.26 kton detector like the LSC in three categories: “New Particles” - experimentally and theoretically motivated; “New Symmetries” - CP-violation and the QCD Axion; And “New Interactions” - Precision Electroweak Physics. See Refs. [4], [5], [11] for further details.

1.1.1 Fluxes in IsoDAR

We consider three fluxes of particles produced in the IsoDAR target for BSM physics searches: the $\bar{\nu}_e$ flux, the neutron flux, and the γ flux from the excitation of nuclei as neutrons are moderated. These fluxes are shown in Fig. 1.2.

The $\bar{\nu}_e$ flux stems from a single beta-decay of ^8Li , which is produced by neutron capture on ^7Li and is well-understood. It peaks at 6 MeV, which puts it above backgrounds from the environment. These are clear advantages over reactor-neutrino fluxes. Interactions in the detector at these neutrino energies are exclusively inverse-beta-decay (IBD) and elastic scattering (ES). Cross sections for these reactions are known with uncertainties at $< 1\%$ at these energies.

Neutrons in the IsoDAR target are primarily produced by spallation interactions of the beam protons with the beryllium target hemispheres. Additional secondary neutrons stem from interactions of the primary neutrons with beryllium in the target and sleeve. We model the processes in the target with Geant4 using an accurate representation of the latest target and sleeve design (see Refs. [12]). We show the resulting neutron energy spectrum in Fig 1.2 (right). Most

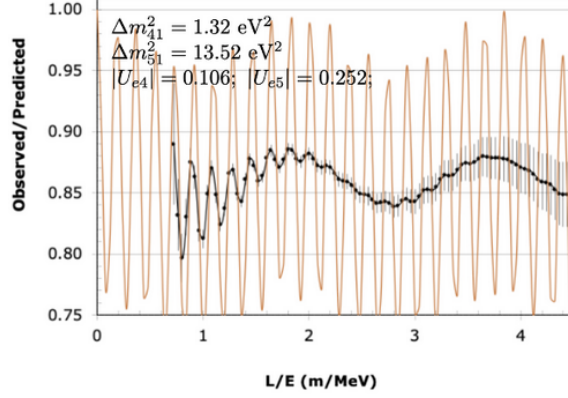


Figure 1.3: *An example of a potential 3+2 signal in IsoDAR, orange—true signature, black—IsoDAR reconstruction with uncertainty shown.*

neutrons capture on the ${}^7\text{Li}$ in the sleeve. To ensure < 5 neutrons per year enter the LSC veto region, the target is further shielded using boron-loaded concrete and steel [13].

The third flux we consider is that of photons as seen in Fig.1.2 (middle). Here, one can observe a line structure that stems from the transitions of excited nuclei and underlying smooth continuum due to bremsstrahlung. Again, the spectrum was generated using Geant4 using the full IsoDAR Target geometry [5].

1.1.2 New Particles: Experimentally and Theoretically Motivated

The original motivation for IsoDAR were the short baseline anomalies in neutrino oscillation experiments. IsoDAR provides a definitive search that is theory-agnostic and can observe signatures depending on L vs. E . The LSC records Inverse Beta Decay (IBD) events with $\bar{\nu}_e$ E resolution of $< 6\%/\sqrt{E}$ and L determination to 40 cm (the 1σ IsoDAR source size). Over 5 years of running, IsoDAR paired with the LSC will collect 1.67 million IBD events. The energy range (cf. Fig. 1.2 (left)) of the neutrinos is 3 to 13 MeV (the cut at 3 MeV is to reduce backgrounds). The baselines (due to the size of the detector) will be 9.5 m to 25.6 m. The capability to resolve several oscillation waves allows IsoDAR to examine models beyond the standard “3+1.” Examples are wavepacket decoherence [14], [15], 3+2 models (Fig.1.3), or 3+1+decay [16].

Another example of IsoDAR’s capability to look for new particles is the “ X ,” which is a low mass mediator that would couple to the photons produced in the target [4]. The X would be a light new particle that decays to $\bar{\nu}\nu$ and would leave a distinct signature above background in the IBD spectrum. Fig.1.4 (left) displays resulting signatures for various masses (see color bar) assuming 0.5% X -to-photon production. The IBD background from $\bar{\nu}_e$ stemming from ${}^8\text{Li}$ decays (gray) constitutes the primary background and has a distinct shape. The sensitivity is depicted in Fig.1.4 (right), where the blue region is excluded in the case of the SM. No existing limits are shown because this search is first-of-its-kind. A 17 MeV X particle is consistent with the Atomki anomaly.

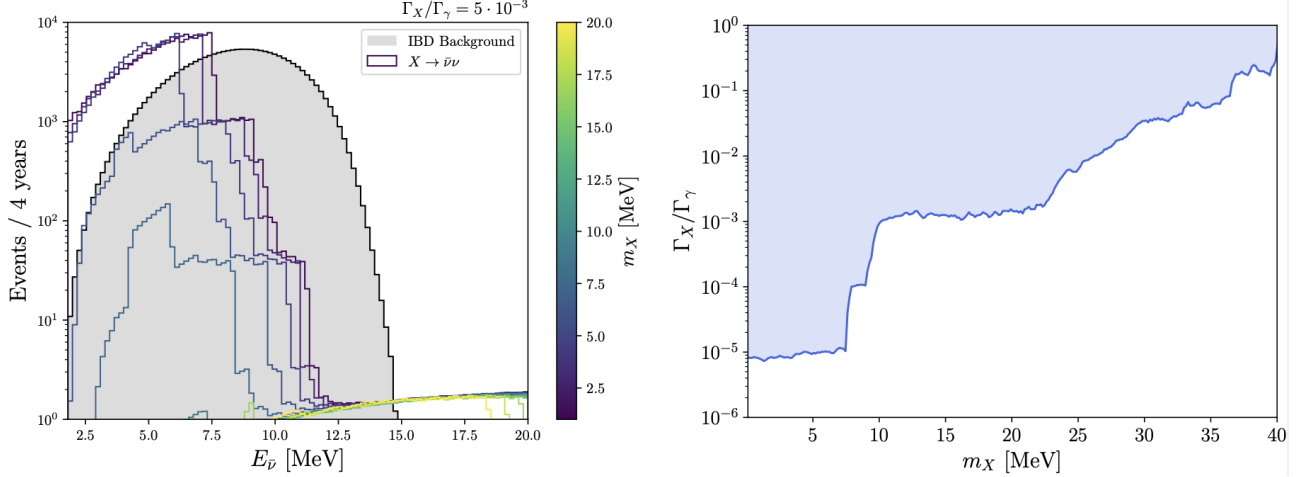


Figure 1.4: *Left: Example $X \rightarrow \nu\bar{\nu}$ signatures for 0.5% photon mixing with ${}^8\text{Li}$ -produced $\bar{\nu}_e$ background (gray). Right: X mass and X -to-photon production ratio 90% CL sensitivity [4].*

1.1.3 New Symmetries: Strong CP Violation and the QCD Axion

The neutron beam/bottle experiment lifetime discrepancy [17]–[20] motivates neutron–dark sector couplings. Through $n \rightarrow n' \rightarrow n$ transitions, we may see neutrons disappearing from the target and reappear in the LSC. The underground environment provides a low background and the LSC’s size further adds to the sensitivity [11]. Alternatively, if the n' are Majorana, then $n \rightarrow n' \rightarrow \bar{n}$ may occur, depositing ~ 2 GeV of energy in the LSC upon annihilation. This is a B violating effect with implications for the early universe [21].

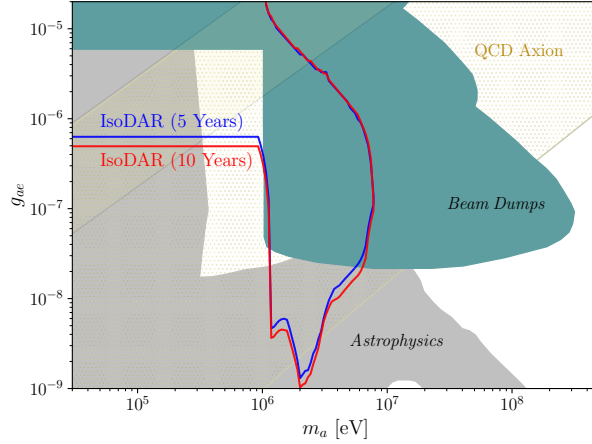


Figure 1.5: *IsoDAR sensitivity for axions (a) with mass m_a coupling (g) to electrons (lines) [5]. Gold dots–axion allowed; Teal–excluded regions; Gray–parameters with astrophysical implications.*

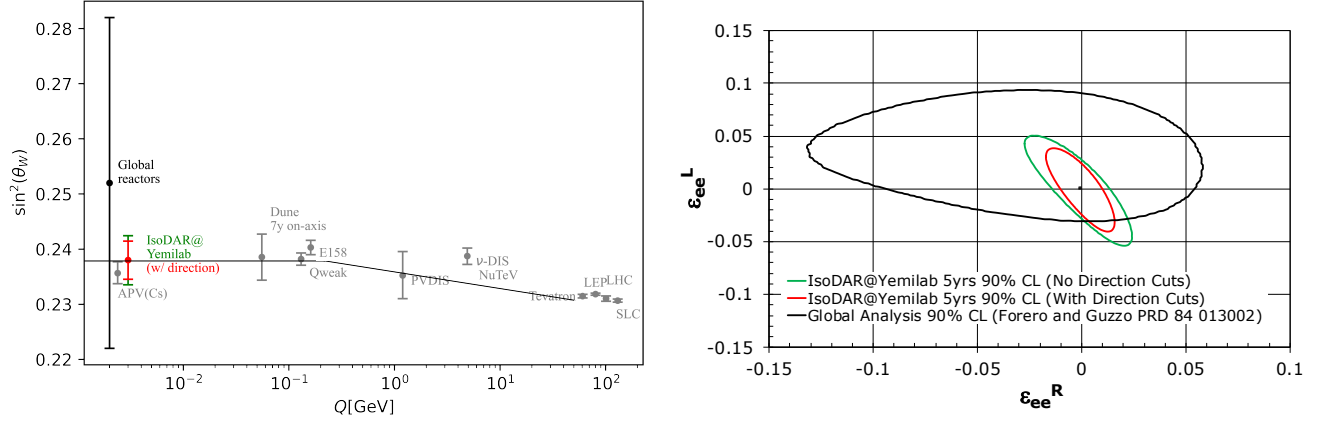


Figure 1.6: *Left: Weak Mixing Angle expectation for IsoDAR compared to present results and the future DUNE expectation. Right: expectation for IsoDAR in NSI parameter space. See Ref. [4].*

The photons and electrons in the target may also couple to axions and IsoDAR can probe uncharted territory with astrophysical and cosmological implications [5]. In Fig. 1.5 we show QCD axions coupling to electrons.

1.1.4 New Interactions: Tests via Precision Electroweak Physics

IsoDAR will record about 7000 elastic scatter events over its 4-year accumulated up-time. This constitutes the world's largest sample at low momentum transfer. LEP and LHC data predict rate and energy dependency very precisely within the standard model [22]. With the normalization determined by the ≈ 1.7 M IBD events in the LSC, we will be able to measure $\sin^2 \theta_W$ with a precision of 1.9% (see Fig.1.6 left).

As a neutrino-nucleon experiment, the observed deviation of NuTeV may stem from unaccounted-for nuclear physics effects; however, numerous possibilities have been investigated, but none fully explain the deviation. Alternatively, the deviation might signal new physics in the neutrino sector. If so, this BSM signature will also manifest in the IsoDAR ES measurement. Fig.1.6, right, presents two expectations for IsoDAR, where the red assumes background reduction from Cherenkov ring identification in LSC, while the green indicates the expectation without this additional information. Statistics limit the outcome, and further running can proceed with IsoDAR and DUNE as it comes online if a NuTeV-like deviation is observed.

The accurately predicted energy dependence of the ES sample enables a precise phenomenological search for non-standard neutrino interactions (NSIs). This powerful search for lepton-lepton couplings complements the lepton-quark coupling searches by the active, global coherent neutrino scattering program. The SM right- and left-handed couplings, g_R and g_L , are altered by NSI corrections for electron flavor antineutrino interactions with electrons (hence "ee") to

$\tilde{g}_R = g_R + \varepsilon_{ee}^{eR}$ and $\tilde{g}_L = g_L + \varepsilon_{ee}^{eL}$. The SM expectation for IsoDAR@Yemilab in the parameter space of these deviations is seen in Fig. 1.6 (right), where red assumes background reduction using Cherenkov light, and green assumes only scintillation light reconstruction. This can be compared to the world result [23] in black, which is dominated by ν_e -electron ES scattering from beam dump experiments and, hence, is rotated with respect to IsoDAR, which has a pure $\bar{\nu}_e$ flux.

1.2 Requirements for the Proton Driver

As shown in Fig. 1.1, the Proton Driver consists of a 60 MeV/amu cyclotron accelerating and extracting 5 electrical milliamperes of H_2^+ , a transport line that strips the H_2^+ ions close to the extraction point, analyzes the stripped beam to monitor the health of the stripping foil, and transports the 10 milliamperes of protons to the target. The target consists of three nested hemispherical beryllium shells, the outermost being 20 cm in diameter, cooled with heavy water flowing around the shell structure. The proton beam is shaped, with quadrupoles and wobbler magnets to produce a distribution that allows for optimal heat transfer to the cooling water. Neutrons produced in the target system are moderated and flood into a roughly-spherical sleeve, about 1 meter in diameter, containing a mixture of beryllium chips and highly-enriched ^7Li . The beta-decay of the ^8Li resulting from the capture of neutrons produces the neutrinos of interest in the experiment.

The principal requirements for the accelerator system are to reliably produce a 10 mA beam of protons in the most efficient manner possible with the lowest possible loss of particles in the acceleration process. Experience from the cyclotron system at PSI [24] are that keeping the total power of beam loss inside the cyclotron vault to less than 200 watts still allows access for component maintenance. Considering that the total beam power is 600 kilowatts, one sees that this is a very stringent requirement.

As mentioned above, Volume 1 of this PDR addresses the physics and engineering aspects of the 60 MeV/amu cyclotron. The final chapter addresses the complex issue of transport and assembly of the large and heavy cyclotron components in the underground environment at Yemilab.

Subsequent volumes will address the details of the beam transport system and the target, along with shielding requirements for the environment of the target including the prevention of fast neutrons from reaching the fiducial volume of the liquid scintillator detector and the underground installation procedure, power and cooling, HVAC, and other site-specific topics.

Chapter 2

Design of the Front End

2.1 The Ion Source

The H_2^+ beam to be injected into the cyclotron and accelerated to 60 MeV/amu will be produced in a filament-driven multicusp ion source which we will refer to as MIST-1. The technical details of this ion source are reported in Refs. [25]–[29] and are summarized here.

2.1.1 Design

For visual reference as we discuss the details of the MIST-1 ion source, a 3D CAD rendering is provided in Fig. 2.1. The ion source source comprises a DI water cooled stainless steel chamber into which hydrogen gas is introduced. A heated tungsten filament emits electrons, which subsequently ionize the H_2 and form a plasma. The plasma is contained by a magnetic field generated by permanent magnets. Ions exiting the source through the front aperture are shaped and guided by the extraction system. These individual components are detailed further below. For reference, the various ion source parameters we will discuss are detailed in Table 2.1.

2.1.1.1 Gas Input

Hydrogen gas is introduced via an inlet in the backplate of the source as indicated in Fig. 2.1. The amount of hydrogen entering the ion source is controlled using a mass flow controller (MKS Instruments Model GV50A) which has a 5 SCCM full range. This system interfaces with the PC control system which is documented in detail in Ref. [29].

2.1.1.2 Ionization by the Filament

After the hydrogen gas is introduced into the chamber, it is ionized to form a plasma using electrons released from a tungsten filament by thermionic emission. The filament is mounted on

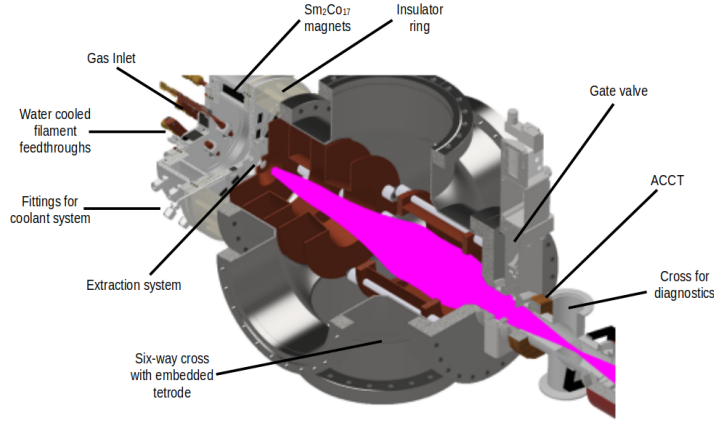


Figure 2.1: A 3D CAD rendering of the MIST-1 ion source.

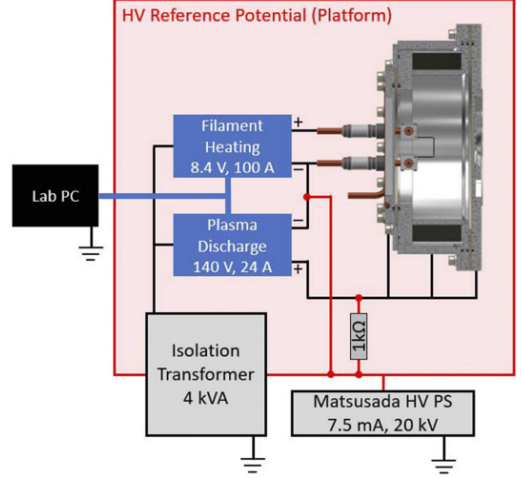


Figure 2.2: Wiring schematic for the ion source. The red square region corresponds to the HV reference potential. Thick blue lines are data cables. Black lines are power cables.

DI water-cooled power feedthroughs in the back plate (cf. Fig. 2.1). The filament is heated by an (8.4V, 300 A max) power supply.

In addition to this power supply which is used to heat the filament, a second power supply is connected to the filament and to the source chamber to maintain a potential difference of 80-140V between them in order to facilitate electron discharge. The source body, back plate, and front plate are all mutually electrically insulated from each other for added flexibility in the electric field shape. A schematic of the wiring of the ion source is illustrated in Fig. 2.2

A significant concern during this stage, which we will quantify in the following section, is the production of ions other than H_2^+ . Of particular concern are H_3^+ , which can be produced via $H_2^+ + H_2 \rightarrow H_3^+ + H$, as well as the production of free protons arising from premature dissociation of the H_2^+ . To mitigate this the length of the plasma chamber is shorter than typical proton sources at 6.5 cm. This corresponds to the lower end of the range for the mean free path of H_2^+ ions within a neutral H_2 gas which we estimate to be between 5-20cm depending on gas input flow rate. For more details on this computation, see Ref. [27].

2.1.1.3 Confinement & Extraction of the Plasma

The plasma is confined using a multicusp magnetic field generated by a set of twelve permanent Sm_2Co_{17} magnets (cf. Fig. 2.1). This creates a field which radially confines the plasma while permitting it to drift towards the extraction aperture located at the front of the source chamber.

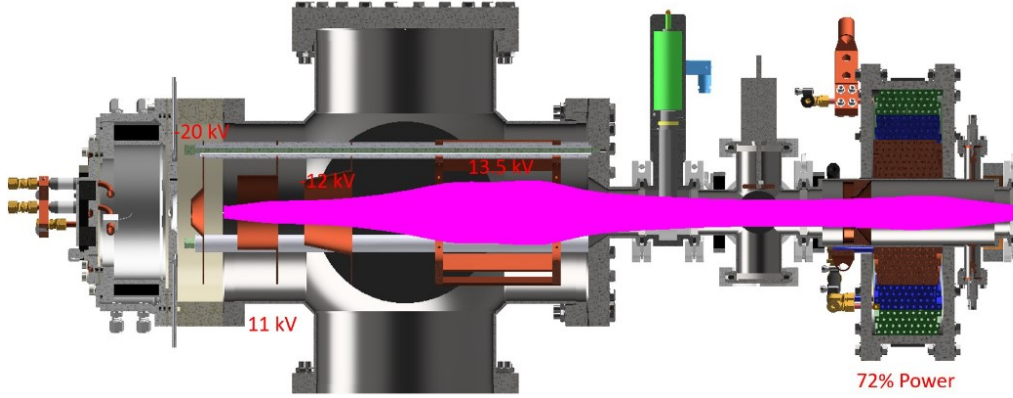


Figure 2.3: Cross section of the extraction system showing the ion beam moving through the extraction system prior to entering the RFQ. Simulation of the extraction system performed by IBSimu and WARP software.

The electrons are then shaped and accelerated out via an extraction system (cf. Fig. 2.1). The extraction system comprises five electrodes which shape and accelerate the ion beam. These include a plasma electrode (+15 kV), a puller electrode (-3 to -20 kV), and three electrostatic lenses – Lens 1 (+10 kV to +15 kV), lens 2 (-3 kV to -15 kV), and lens 3 (+10 kV to +15 kV). The RFQ entrance flange is held at ground potential. We simulated beam formation and shaping in the extraction system with the IBSimu package [30], which performs 3D simulations including space charge. Due to the computational resources needed to perform full 3D simulations in IBSimu, we adopted a hybrid IBSimu (for the plasma modeling)/WARP (for the beam transport) [31] model for the final design. We show example trajectories in Fig. 2.3.

2.1.2 Performance

2.1.2.1 Goals & Measurement Methods

In this section we summarize the latest measured results as well as discussing the results of several optimizations that have been thus far performed as well as several that remain to be performed. The ion source target parameters that will be required for IsoDAR to achieve the planned decisive results for a sterile neutrino search include the following benchmarks:

- High current: ≈ 10 mA of H_2^+
- High purity: H_2^+ fraction $> 80\%$
- Low emittance: $< 0.1\pi$ -mm-mrad (1-RMS, normalized)
- Ability to run continuously in DC mode

Characterization of the ion source is done using a short diagnostic beam line. This test beam line comprises two Faraday cups, a dipole magnet with separation slits, and a pair of Allison emittance scanners. The total beam current is measured using the first Faraday cup located posterior to the extraction system. The dipole magnet with separation slips separates the ions by mass and passes them to the second Faraday cup which, in conjunction with the Allison scanners, measures each species horizontal and vertical emittances.

2.1.2.2 Optimization of Ion Source Parameters

The ion source is designed such that several parameters can be varied in order to optimize the magnitude, purity, and emittance tightness of the current from the ion source.

- H₂ input flow rate
- Filament discharge voltage
- Filament discharge current
- Filament size, shape, & position (*Optimization not yet studied*)
- Permanent magnet type (*Optimization not yet studied*)

Table 2.1: A summary of the parameters for the MIST-1 ion source.

Parameter	Nominal Value
Plasma chamber length	6.5 cm
Plasma chamber diameter	15 cm
Permanent magnet material	Sm ₂ Co ₁₇
Permanent magnet strength	1.05 T on surface
Front plate magnets	12 bars (star shape)
Radial magnets	12 bars
Back plate magnets	Four bars in three rows
Front plate cooling	Embedded steel tube
Back plate cooling	Embedded copper pipe
Chamber cooling	Water jacket
Water flow (total)	≈2 L/min
Filament feedthrough cooling	Water cooled
Filament material	Water mixed with Cu and Ni
Filament diameter	≈0.8 mm
Discharge voltage	Max. 150 V
Discharge current	Max. 24 A
Filament heating	voltage Max. 8 V
Filament heating	current Max. 100 A

H₂ input flow optimization. Three series of optimizations on the input gas flow rate have been performed. The three series differ in how the filament discharge voltage is managed. In the first series, the PID loop which stabilizes discharge was disabled allowing the discharge current to rise to the source steady-state value and then stabilized at that value by reengaging the PID. In the second series, the discharge current was kept fixed at 4A. In the third series, the discharge current was reduced to keep the total extracted current fixed at 1.25 mA. Under each of these three conditions, the gas input rate was varied from 0.25-1.25 SCCM. This study demonstrates a general trend of greater H₂⁺ production at higher discharge currents and, as theoretically expected, a higher fraction of H₃⁺ with higher flow rates.

Filament discharge voltage optimization. Two series of filament discharge voltage optimizations have been performed differing in how discharge current is managed. In the first, discharge current is permitted to freely find a steady state using the same method as used in the flow optimization described above. In the second, the discharge current was fixed at 4 A.

Filament discharge current optimization. One series of current optimizations was explored in which the flow rate and discharge were kept constant while discharge current was varied from 2 to 8 A. No strong dependence on current was observed.

2.1.2.3 Latest Optimized Results

To date, only an incomplete optimization of the ion source has been performed. As such, parameters which simultaneously meet all the target goals have not yet been fully identified. The ion source's peak performance to date varies, therefore, depending on which of the performance metrics is optimized. Optimization has been performed for maximum total current density, maximum H₂⁺ purity, and a hybrid option optimizing for the maximum H₂⁺ current density with the constraint that H₂⁺ be dominant.

Highest total current density: 41 mA/cm² with 31% H₂⁺ purity.

Highest H₂⁺ purity: 76% purity with 11.4 mA/cm² total current density.

Highest H₂⁺ current density with H₂⁺ dominant: 10.4 mA/cm² with 62% purity.

With current optimizations and a 4mm aperture, the ion source is capable of delivering approximately 1.1 mA of H₂⁺ with 76% purity. With an 8 mm aperture this corresponds 4.4 mA. This is a world leading result and is only about a factor of 2 short of target.

The main bottleneck for increased beam current was the extraction system, which was designed for initial testing and commissioning. We have recently replaced it with the version presented in this chapter. Our high fidelity simulations suggest that the new extraction system will be able to handle the nominal beam current. Measurements are planned for summer 2024.

2.2 The Low Energy Beam Transport

The low energy beam transport line (LEBT) serves the purpose of connecting the ion source to the RFQ. The LEBT steers and shapes the beam, guiding it into the RFQ. The LEBT also provides a location at which to take beam diagnostics. The requirements for the LEBT are:

1. Transport beam with minimal losses,
2. Provide space for diagnostics,
3. Match the beam to the RFQ,
4. Provide safety mechanisms for personnel and machine protection.

Details of the LEBT design and performance were given in Refs. [32]–[34] here we summarize and update these.

2.2.1 Design Overview

At this stage, ions emerge from the ion source. The beam now passes through a gap surrounded by a series of six electrodes arranged axially within a six-way cross (see Fig. 2.1). These six electrodes can have their voltage optimized in order to best match the parameters for acceptance into the RFQ. A conical flange is connected to the end of the six-way cross. The conical shape minimizes beam loss on exit.

Following the six-way cross lies a diagnostic segment. A gate valve separates the six-way cross from this segment. The diagnostic section comprises a second cross, which can be used for additional vacuum attachments, diagnostic readouts, and a chopping electrode. The diagnostic section also includes a solenoid and two magnetic steerers which can be used for additional beam tuning. A flange in place toward the end allows space for an ACCT which characterizes the beam immediately prior to entering the RFQ. The diagnostic segment is illustrated in Fig. 2.3.

2.2.2 Beam Steering & Chopping

The diagnostic segment also serves to steer the beam into the RFQ or terminate the beam as needed. Even small, sub-millimeter misalignment can prevent efficient injection of the beam into the RFQ. In order to ensure that the beam enters the RFQ at both the correct position and angle, two magnetic steerers and a solenoid are placed around the beamline. These are controlled independently by an external power source to produce tunable dipole fields which

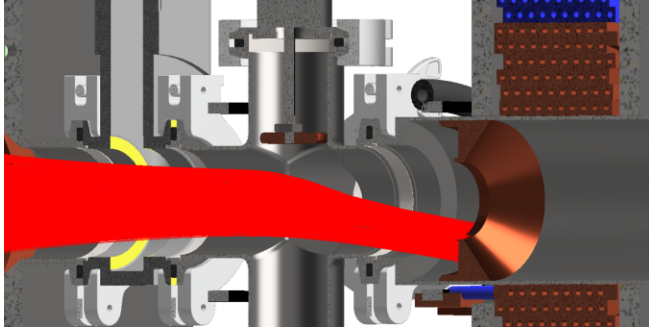


Figure 2.4: CAD model of the LEBT diagnostic segment with beam simulation (red) overlaid. If the copper electrode (top) is held at adequate potential the beam is pushed off its center course and terminates on the copper ring.

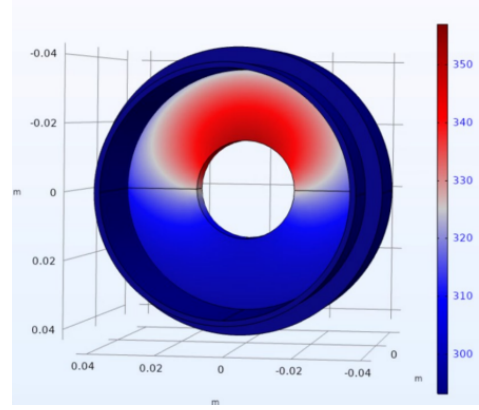


Figure 2.5: COMSOL simulation of the beam terminating on the copper aperture surrounded by the steel beampipe, with copper water cooling channel on the exterior.

optimize beam entry into the RFQ. The optimal fields were calculated using COMSOL and Warp. These are discussed further in the following section.

In order to control the amount of power delivered from the ion source, a beam chopper is built into the cross of the diagnostic segment to allow for a duty factor in an otherwise DC beam. The beam chopper is built into the cross in the diagnostic section. The chopper comprises a copper ring surrounded by a steel beampipe which in turn is surrounded by a copper water cooling jacket. The copper ring can be put at a high potential relative to the cross, which is grounded. If the potential is sufficiently high the beam can be diverted such that it terminates. See Fig. 2.4. This method permits control over the amount of power delivered to the RFQ without disrupting the plasma itself.

A 12 mA beam of 15 keV particles fully terminating on the beam stop corresponds to ~ 180 W power delivered. We need to ensure that the dump is capable of dissipating this amount of power. The system was modeled assuming a water cooling line at room temperature. To be conservative, the simulation was run using four times the actual anticipated beam power, i.e. 720 W. The beam dump never rose above 360 K in our simulation, significantly below the melting point of copper. The COMSOL simulation is shown in Fig. 2.5

2.2.3 Beam Dynamics

Beam simulations are performed in order to characterize the performance of the LEBT with the ultimate goal of ensuring that beam's Twiss parameters matches the desired input parameters for the RFQ.

Beam simulations for the LEBT have been performed using IBSimu and Warp. IBSimu provides a more accurate plasma model, but is computationally intensive and so was used only for the region by the ion source where the plasma is extracted and the density is thus high, requiring this accuracy. IBSimu is used for the first several mm after the extraction aperture where density remains high. After this, and for the remainder of the downstream region of the LEBT, the distributions from IBSimu are handed off to Warp which provides accurate results for the lower density regions of the beam with less computational burden.

For the IBSimu simulations a 12 mA beam composed of 80% H_2^+ , 10% H^+ , and 10% H_3^+ was used. This provides ample current for IsoDAR assuming 50% global transmission efficiency while using current from the ion source that has already been empirically demonstrated. As illustrated in Fig. 2.6 and in Table 2.2 the LEBT is able to match the required input parameters for the RFQ. Moreover, as illustrated in Fig. 2.7 this match is achieved with emittance that surpasses that used for baseline RFQ simulations.

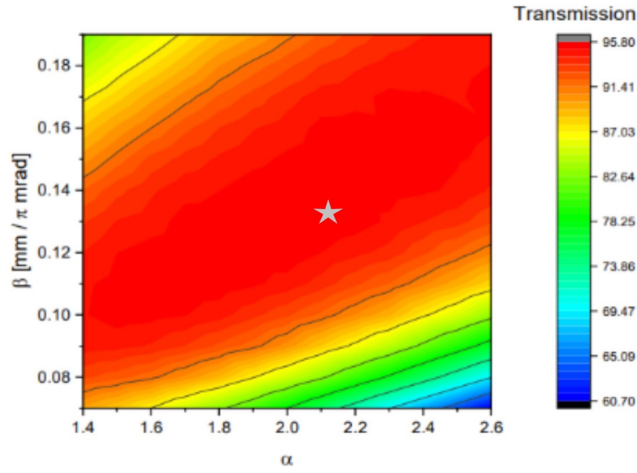


Figure 2.6: A temperature plot showing the Twiss parameters required for optimal transmission through the RFQ. The indicated point shows the parameters at the end of the LEBT.

Table 2.2: A comparison of LEBT Twiss parameters and baseline RFQ parameters.

Parameter	LEBT Output	Baseline
Norm. RMS Emitt.	0.175π mm-mrad	0.3π mm-mrad
α	1.3	1.0
β	0.13 mm/mrad	0.17 mm/mrad

2.3 The Radiofrequency Quadrupole

The H_2^+ beam coming from the LEBT is injected into a Radio Frequency Quadrupole (RFQ) that is partially embedded in the cyclotron yoke. A schematic of the RFQ and cyclotron can

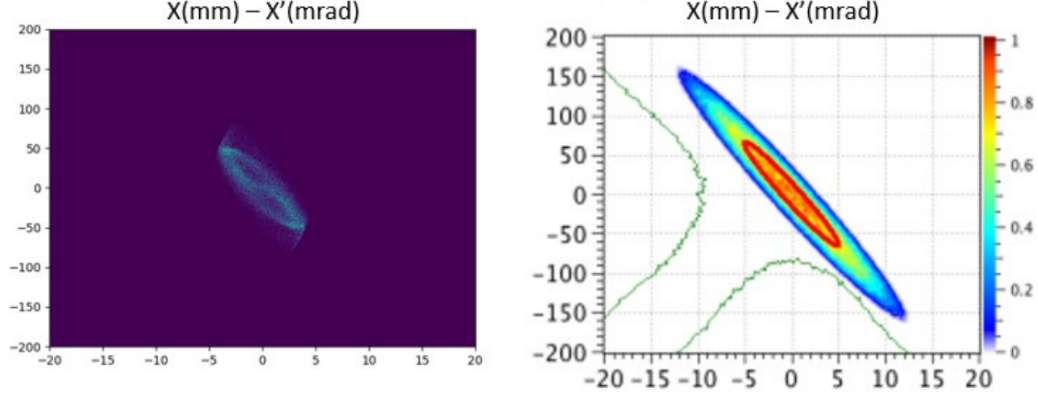


Figure 2.7: Phase space from the LEBT simulation (left) vs phase space for ideal beam input to the RFQ (right).

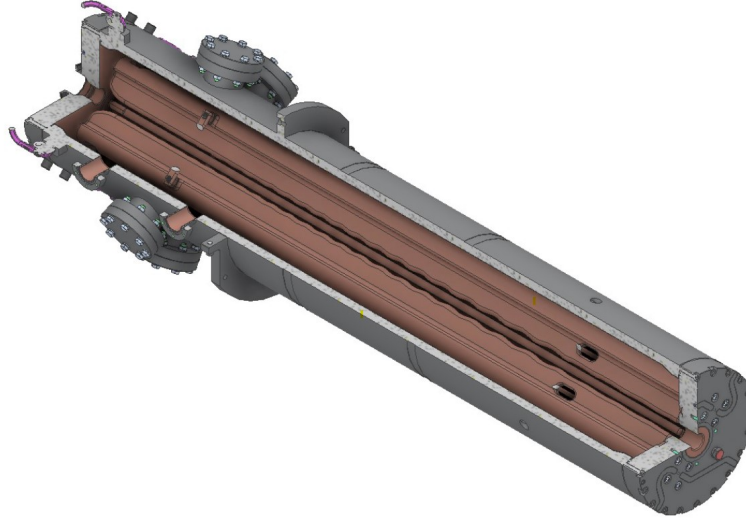


Figure 2.8: Cut view of the IsoDAR RFQ. In the split-coaxial design, vanes are attached to the front and end plates rather than radially to the mantle.

be seen in Fig. 3.1 where only about a third of the RFQ is visible above the top surface of the cyclotron. We show a cut view of the RFQ in Fig. 2.8. Of note are the small diameter of the RFQ (27.6 cm) while operating at a low resonant frequency of 32.8 MHz. This is achieved by utilizing the so-called “split-coaxial” mode where the vanes are attached longitudinally at the entrance and exit flanges instead of radially at the mantle. The main operating parameters of the RFQ are listed in Tab. 2.3. The RFQ accelerates only moderately from 7.5 keV/amu to 35 keV/amu and acts mainly as a very efficient buncher. This leads to a conservatively estimated power consumption of < 6 kW.



Figure 2.9: Modes of the mechanical deformation of the RFQ vanes. The frequencies are 18 Hz and 25 Hz.

2.3.1 Technical Design

The technical design was presented in Refs. [35]–[37] and the optimization of the RF loop coupler in Ref. [38]. The thermal properties and cooling considerations were presented in Ref. [39]. An optimization scheme using machine learning was presented in Ref. [40].

In terms of mechanical stability, our analyses show two quarter wave modes which are associated with the choice of a split-coaxial resonator. The addition of bridges between opposite vanes (see Fig. 2.9) significantly reduces detuning due to the Lorentz force with mechanical frequencies around 18 Hz and 25 Hz.

2.3.2 Beam Dynamics

Beam dynamics studies were performed of the full 3D particle distribution resulting from the LEBT simulations going through the RFQ, including the effects of the entrance gap and asym-

Table 2.3: A summary of the design parameters for the RFQ.

Parameter	Nominal Value
Diameter	27.6 cm
Frequency	32.8 MHz
Tuning range	± 270 kHz
Q simulated	2800
Shunt impedance R_p	4.9 k Ω /m
Input Energy	7.5 keV/amu
Output Energy	35 keV/amu
Duty factor	100% (cw)
Power	< 6 kW
Cooling	DI Water channels in tank and vanes

Table 2.4: RFQ output beam parameters.

Parameter	Nominal Value
ε_x (1-RMS, norm.)	0.54 mm-mrad
ε_y (1-RMS, norm.)	0.52 mm-mrad
ε_z (1-RMS, norm.)	0.114 MeV-deg
Phase width (1-RMS)	40°

metry (due to the split coaxial design) and the exit gap and asymmetry. Fine tuning of the phase of the exit gap (i.e. tuning the length of a drift preceding the exit gap), leads to final output beam parameters listed in Tab. 2.4.

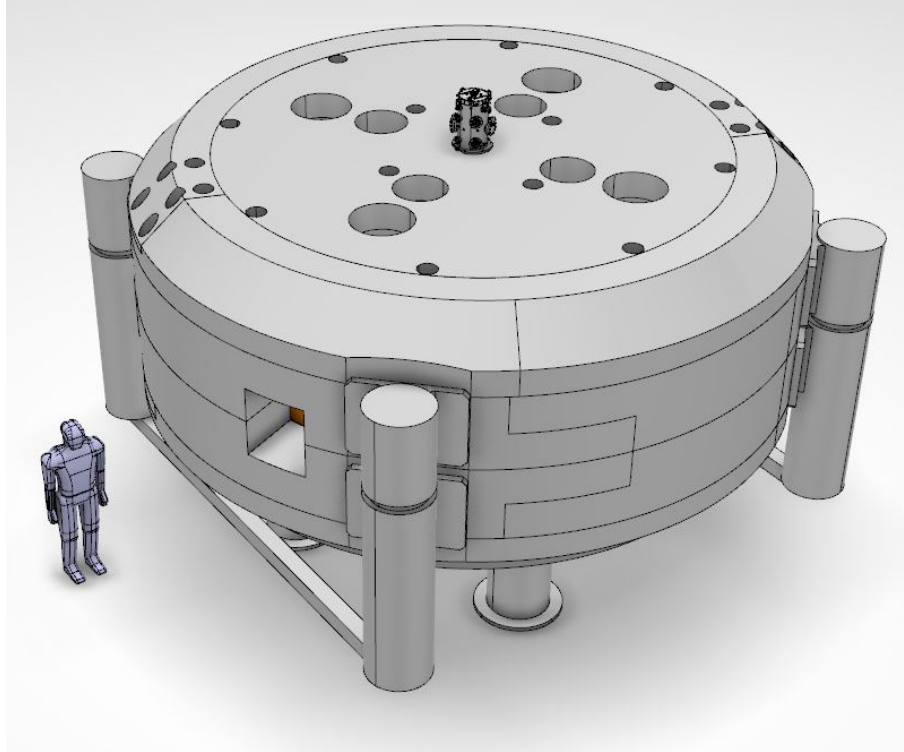


Figure 3.1: Isometric view of the cyclotron

Chapter 3

Design of the Cyclotron

In this section we describe the details of the cyclotron design at the level of a preliminary design report.

3.1 Magnet Yoke

The magnet design presented here will necessarily be modified for a final design, as the specific details of the extraction orbit and all required extraction elements have not been finalized.



Figure 3.2: C400 on the milling machine, C230 in front of it.

The engineering design of the IsoDAR magnet benefits from the experience gained by IBA in the fabrication of its C400 cyclotron, which is slightly larger, at 7 meters outer diameter.

3.1.1 Design and fabrication of the cyclotron magnet

The cyclotron is divided in the same fashion as the C400, into smaller parts facilitating transport to the site. The magnet is split radially and will be assembled on site. The vacuum chamber is split in 3 (self-centering) parts along its height, the vacuum tightness is ensured by 2 axial O-rings at each interface except for the interface between the upper and lower chambers where 2 radial O-rings are used. An exploded view of the upper and lower parts is shown in Figs. 3.3 and 3.4. The materials used for the magnet parts is cyclotron steel (the exact composition shall be determined after a detailed physics study), the vacuum chambers will be made of stainless steel.

An overview of a cut in the cyclotron is shown in Fig. 3.5. The external and vacuum disks are connected to each other as well as to the flux return using specific bolts (such as the Superbolt from Nord-Lock). The poles are split in several parts and an easily removable part should be added in the next iteration to ease the mapping and possibly improve the magnetic performance. A detailed view of the cyclotron components is shown in Fig. 3.6.

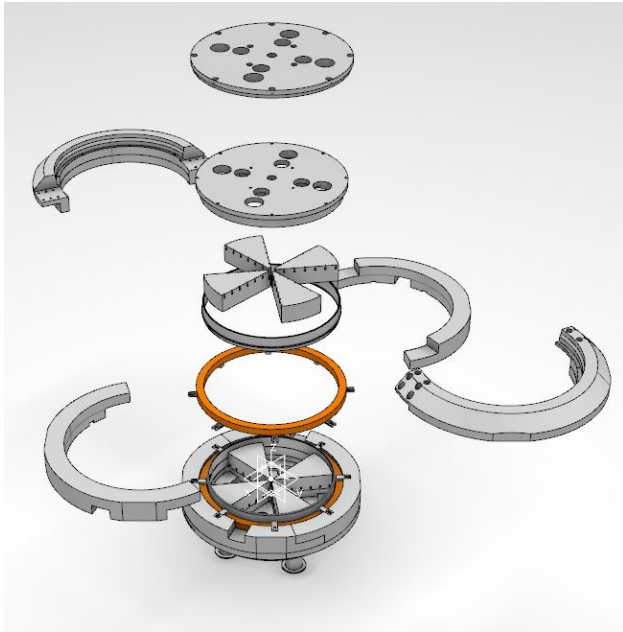


Figure 3.3: Cyclotron upper steel exploded.

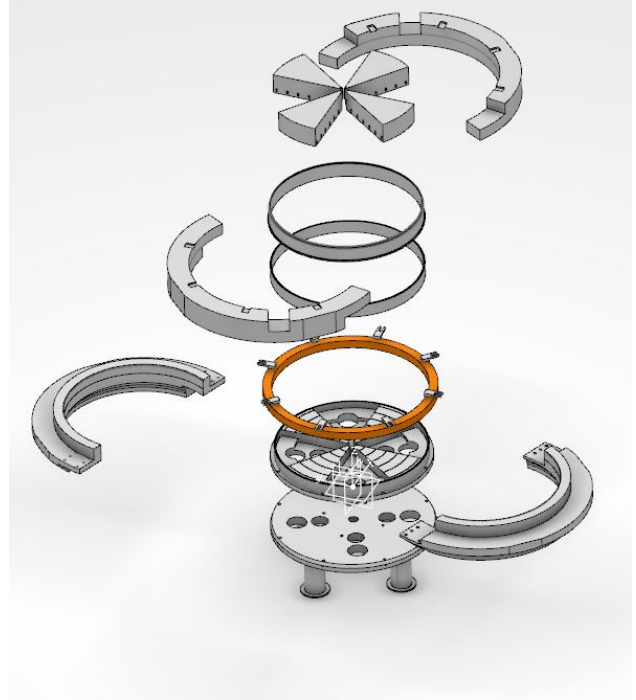


Figure 3.4: Cyclotron lower steel exploded.

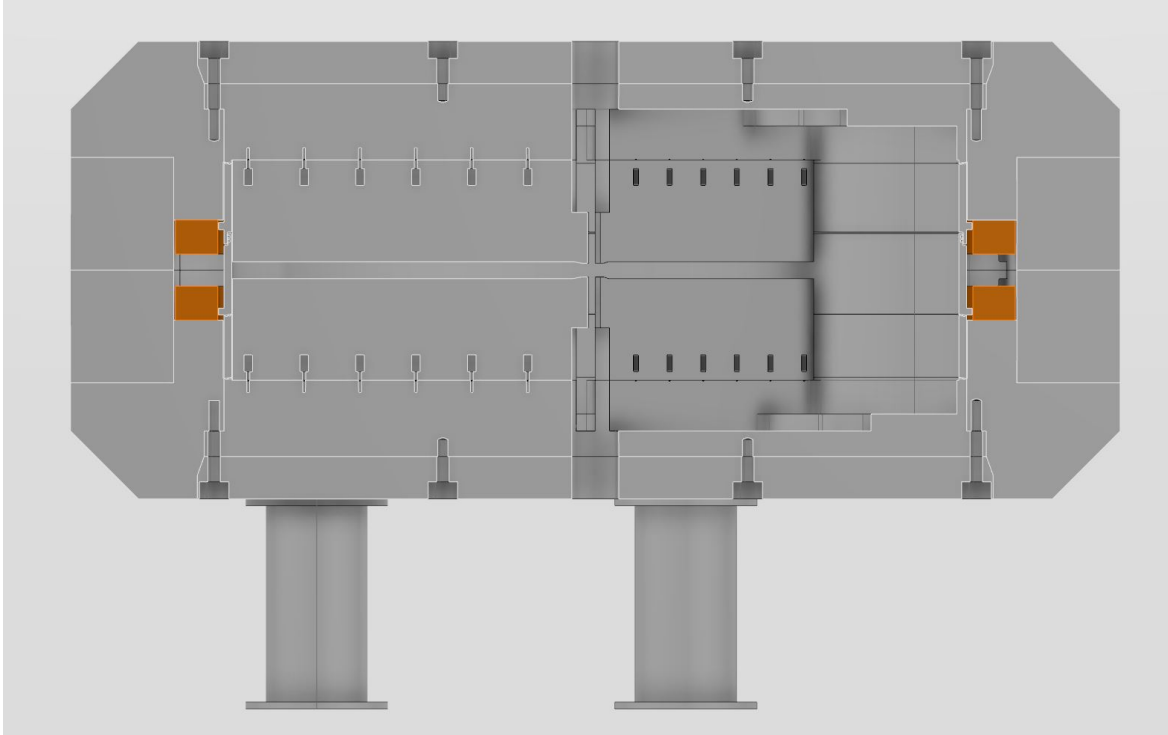


Figure 3.5: Cyclotron cut view

Name	Mass (Metric Ton)	Dimensions (mm)
Upper and lower external disk	30	Ø4700*250
Upper and lower internal disk	36	Ø4620*463
Upper and lower flux return (1 and 2)	36	3100*1950*1015
Upper and lower median plane flux return (1 and 2)	29	3100*1950*705
Upper and lower pole	7	2013*1290*600

Table 3.1: Yoke part properties

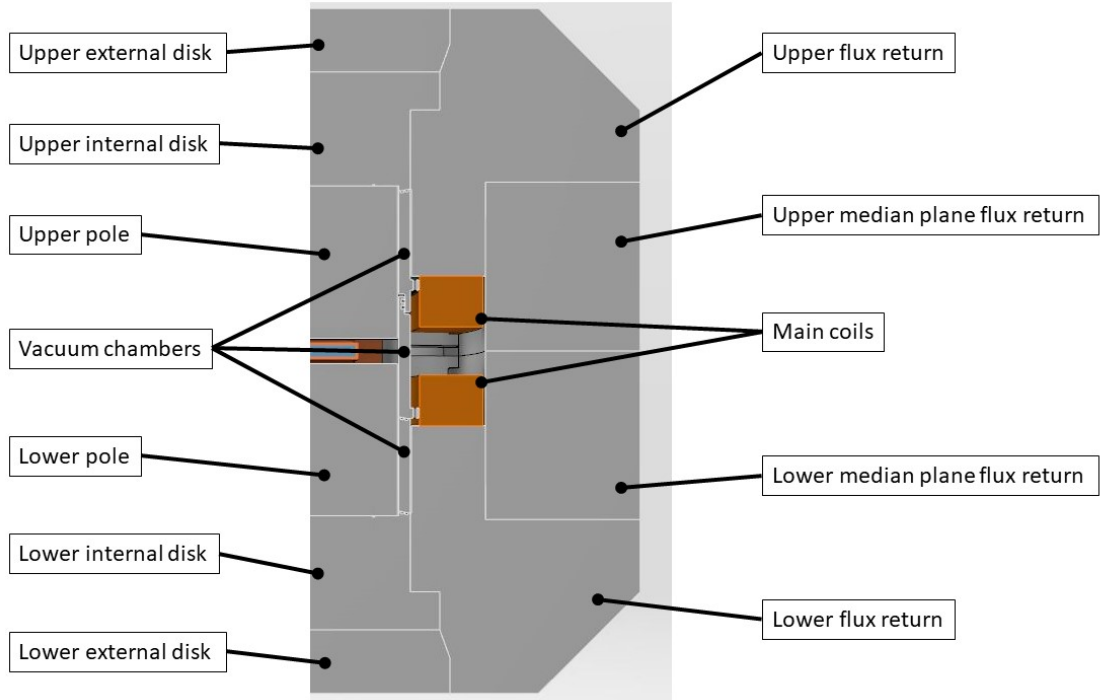


Figure 3.6: Cyclotron detailed cut view

Table 3.1 gives some more information regarding the yoke parts.

3.2 Interface with the RFQ

The RFQ will be outside of the cyclotron's vacuum, therefore a vacuum sleeve will be used to ensure the integrity of the cyclotron's vacuum. This sleeve will be fixed on top of the upper external disk and the vacuum sealing will be done radially on the upper internal disk (as seen in figure number 3.9). The O-rings could have a cross section diameter of 8mm and an inner diameter of 305mm.

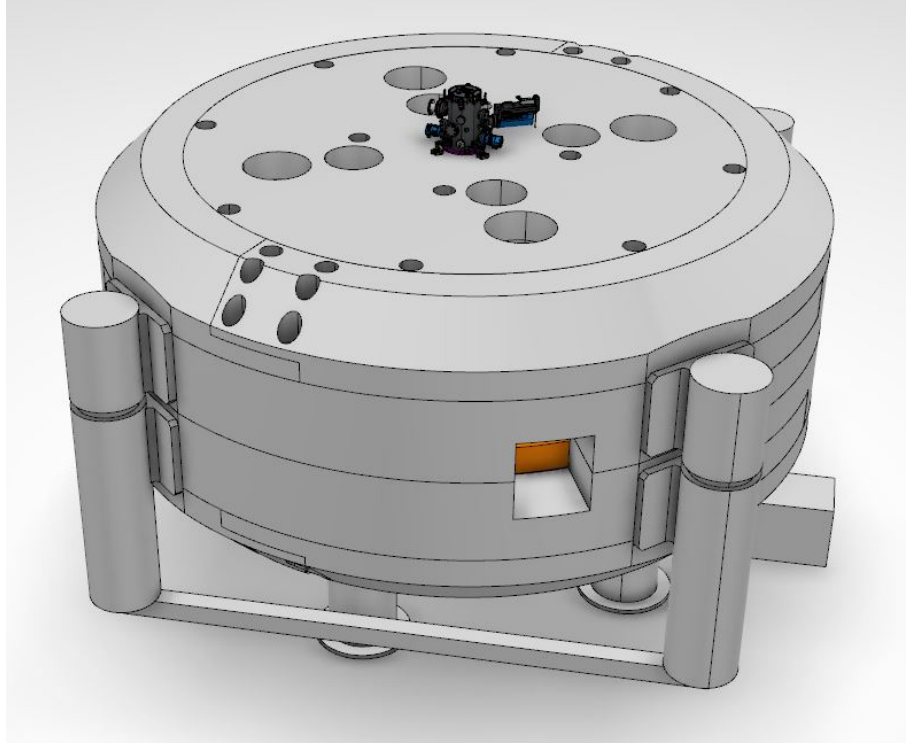


Figure 3.7: RFQ overview

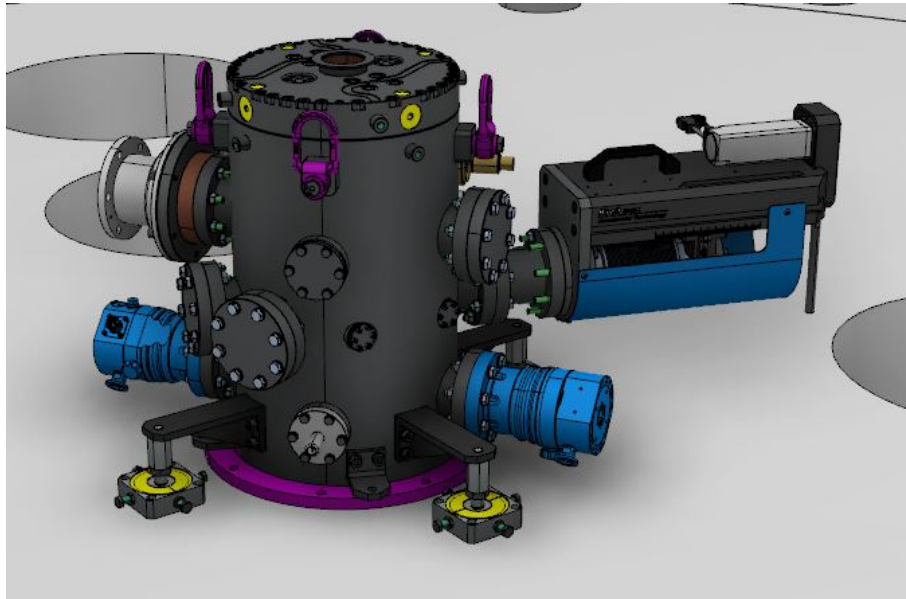


Figure 3.8: RFQ zoom

In order to allow some adjustment, the RFQ sleeve allows a rotation of 5mrad around the lower O-ring contact patch (discussed with the manufacturer of the RFQ). The RFQ sleeve is as thin as possible to avoid any loss in magnetic field in the central region (hence the O-rings in the Yoke parts).

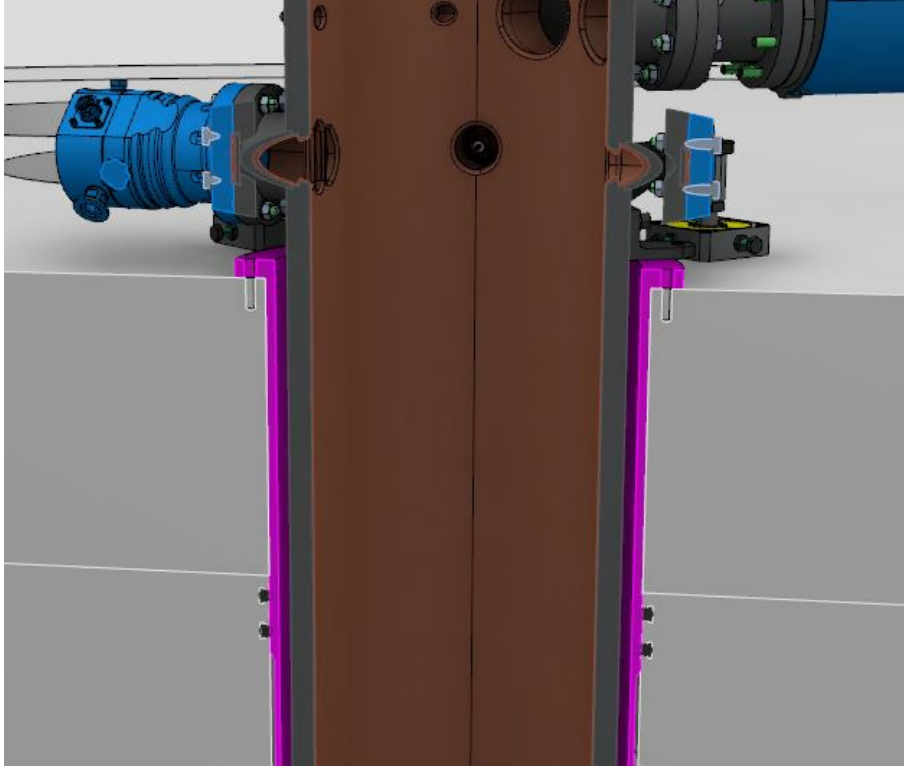


Figure 3.9: RFQ cut section 1

Fig. 3.10 shows that the vacuum sealing will be done at the bottom of the RFQ using a thick O-ring (diameter 10 mm) which will be compressed by the RFQ's weight (≈ 3000 N). The dimensions of the vacuum sleeve are listed in Tab. 3.2.

The adjustment feet shown in Fig. 3.8 are fixed to the cyclotron yoke and allow the following alignment modifications through four sets of four set screws one and vertical adjustment nut:

- Rotation: $\pm 5^\circ$
- Tilt: ± 5 mrad
- Lateral movement: ± 1 mm

In addition to this fine-tuned alignment, a coarse alignment step is envisioned during the initial assembly and commissioning procedure.

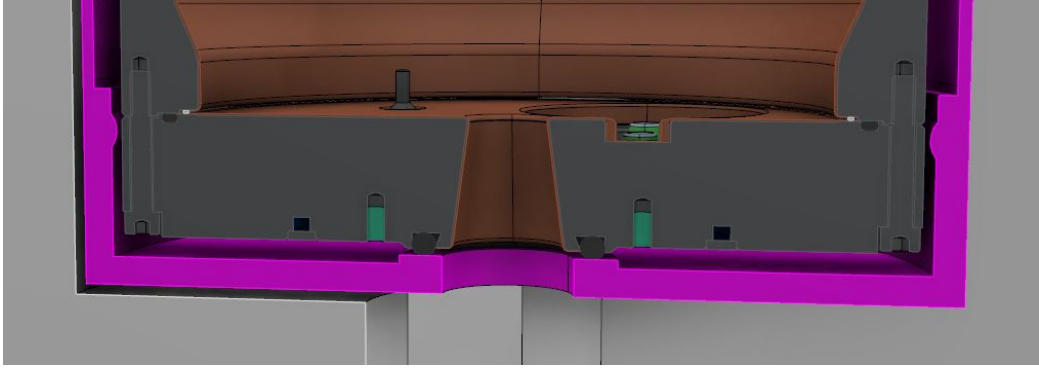


Figure 3.10: RFQ cut section 2

3.3 Central Region

The injection system design is a crucial component to achieve the highest beam current. Our design balances injecting the H_2^+ molecule at high energy against avoiding the use of complex high-voltage platforms. Higher energy injection mitigates space charge and to reduces geometrical (non-normalized) emittance. An energy of 35 keV/amu was selected which determined the output energy of the RFQ. As in commercial cyclotrons, an axial injection system based on a Spiral Inflector (SI) will be used to bend the beam from the axial direction to the median plane. This concept is visualized in Figure 3.11 using trajectories calculated with OPAL [42]. The exit point of the spiral inflector is also the starting point of acceleration in the Central Region (CR) of the cyclotron. The central region and the spiral inflector have to be designed carefully and together because they have strong interplay. This procedure has already been performed and tested for the injection tests during the summers of 2013 and 2014 at the Best Cyclotron Systems Inc. (BCSI) laboratory in Vancouver. In the following subsection, we will describe the design process of the central region for the BCS test stand cyclotron followed by a preliminary design for the full IsoDAR machine.

3.3.0.1 Spiral Inflector Design

The axial injection of the ionized beam into a cyclotron is realized using an electrostatic device called a spiral inflector, which consists of two curved electrode deflectors (see Figure 3.11). The

Table 3.2: Vacuum Sleeve Dimensions.

Name	Value
Height	1030.5mm
Outer diameter	304.55mm
Inner diameter	296.55mm
Weight	18kg

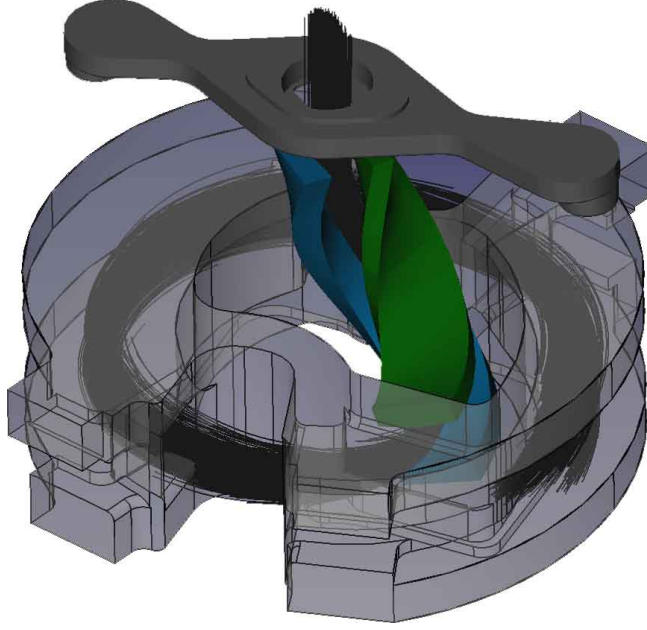


Figure 3.11: CAD rendering of the spiral inflector and particle trajectories for early tests at Best Cyclotron Systems Inc. [41]. The positive and negative electrostatic deflectors are shown in blue and green respectively. The cyclotron magnetic field in this image is directed vertically upwards. Particles enter the spiral inflector via the rectangular grounded collimator (solid gray) and are guided into the cyclotron mid-plane by means of the cyclotron magnetic field and the electrostatic potential between the electrodes. The copper housing (transparent gray) isolates the spiral inflector from the RF fields driving the cyclotron.

electrostatic potential between these electrodes is able to bend the beam 90° from the axial line to the median plane of the cyclotron. The helical trajectory of the beam is determined both by the shape of the electrodes (electric field) and the magnetic field of the cyclotron as the beam is bent into the median plane. The applied voltage depends on the velocity of the beam as well as the rigidity of the ions.

The spiral inflector tested at BCSI (shown in the photograph in Figure 3.12) was designed to mimic the conditions required for the IsoDAR inflector, its primary defining characteristic being the 15 mm gap between the electrodes. Compared to other similar designs, this is rather large because it has to take into account the larger beam size due to space-charge effects and the higher rigidity of H_2^+ . Due to the large distance between the electrodes, the SI occupies a volume in which the magnetic field components' variation is not negligible, as it is assumed in the analytical treatment of the spiral inflector. This effect has to be carefully taken into account in order to shape correctly the spiral inflector electrodes and to avoid the introduction of a high energy-spread during the beam transport through the device. The spiral inflector has a copper housing that surrounds the electrodes to minimize the interaction between the electric fields generated by the dees and the electrostatic fields between the electrodes. To minimize beam striking the uncooled electrodes, a water-cooled, grounded, rectangular collimator shields the spiral inflector entrance.

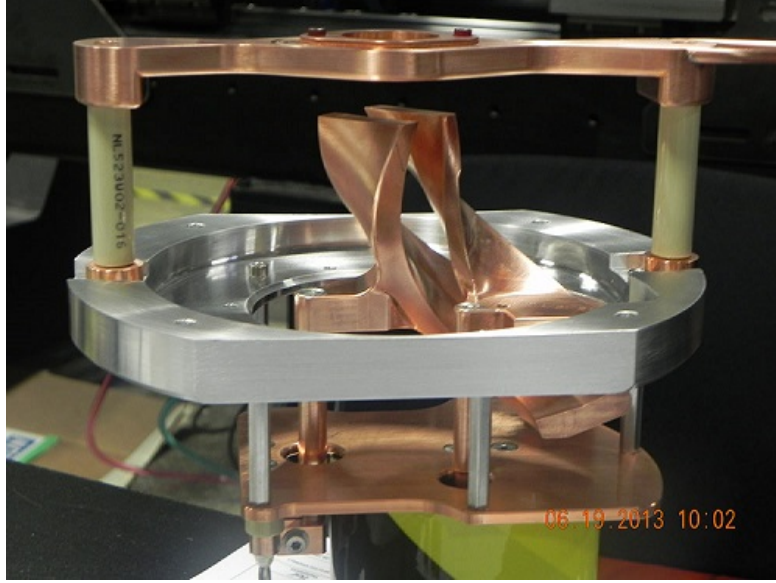


Figure 3.12: Photograph of the spiral inflector used during the tests at Best Cyclotron Systems.

The preliminary design of the spiral inflector called for a nominal voltage of ± 11 kV and a tilt angle of 16° for optimal beam injection at 60 keV. The total height of the device was approximately 80 mm. These parameters were found by using a MATLAB code based on an analytic theory for spiral inflectors. The electrode shape was calculated using VectorFields OPERA. This design was later modified to account for some effects due to fringe fields on the electrodes. One of these modifications was to reduce the overall length of each electrode by 5 mm.

First turn acceleration is achieved by the dee tips extending into recesses in the spiral inflector housing. The shapes of the dee tips and the spiral inflector housing have been designed to guide the particles from the spiral inflector exit to the acceleration region while providing the necessary energy gain and beam focusing.

The final OPERA simulation (neglecting space-charge effects) of the spiral inflector was able to transport a 60 keV beam with a normalized rms emittance of 0.62π -mm-mrad at a transmission efficiency of 100%. This was corroborated by the tests performed at BCSI [41].

The main differences between the BCSI test stand design and the IsoDAR design are:

- The IsoDAR cyclotron will be equipped with 4 accelerating RF cavities, while the test cyclotron used only 2 cavities.
- The harmonic mode (and the frequency) will be decreased from 6th harmonic (49.2 MHz) to 4th harmonic (32.8 MHz).
- The injection energy will be increased from 30 keV/amu to 35 keV/amu.

- The spiral inflector gap will be increased from 15 mm to 16.5 mm to accommodate a larger beam.

3.4 Vacuum Chamber

The vacuum enclosure is composed of 5 parts : the upper and lower internal disk and 3 vacuum chambers. The vacuum sealing is done using 2 metallic O-rings per interface (from Omniseal [<https://www.omniseal-solutions.com/>] for example) except for the radial interface where Polymer O-rings could be used. The interface for the accessories will be done using a sleeve design and radial O-ring, described in the figure hereunder.

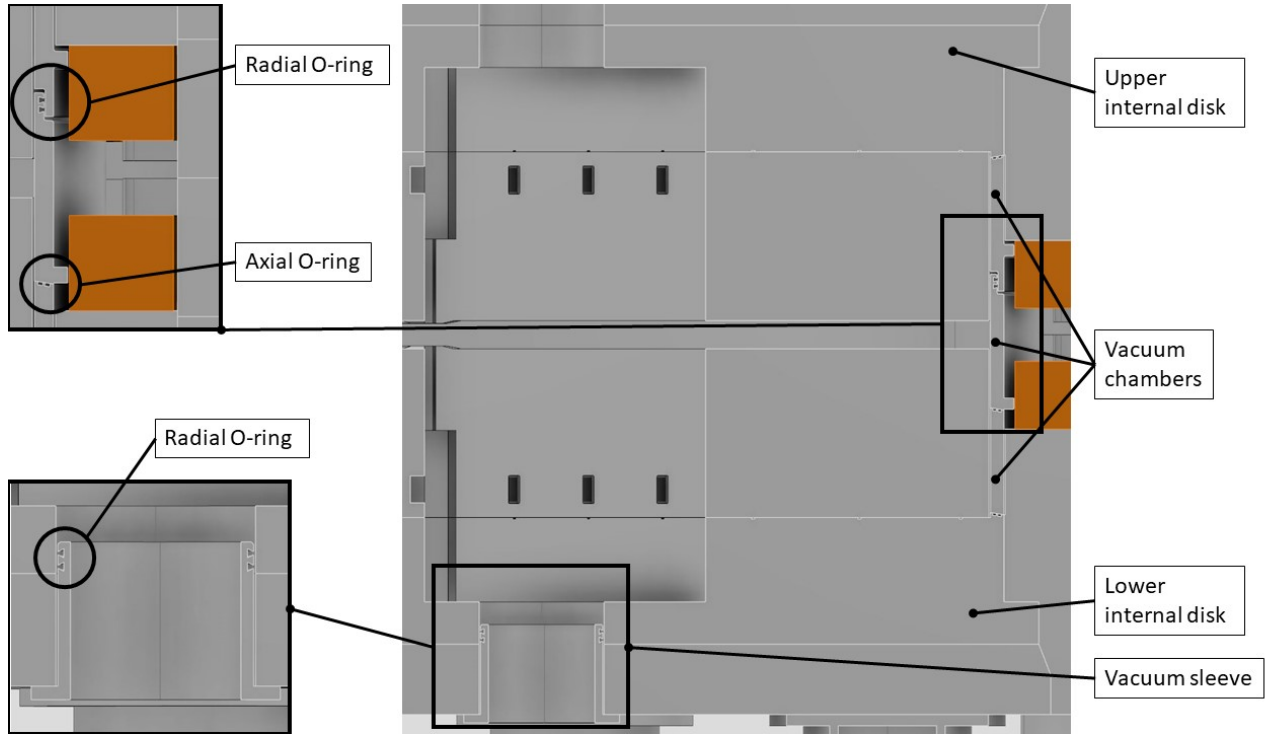


Figure 3.13: Cyclotron vacuum chamber details

Name	Mass (Metric Ton)	Dimensions (mm)
Upper and lower internal disk	36	Ø4620*463
Upper vacuum chamber	2.3	Ø4452*483
Lower vacuum chamber - median plane	2.3	Ø4452*483
Lower vacuum chamber - internal disk	1.8	Ø4386*380

Table 3.3: Vacuum part properties

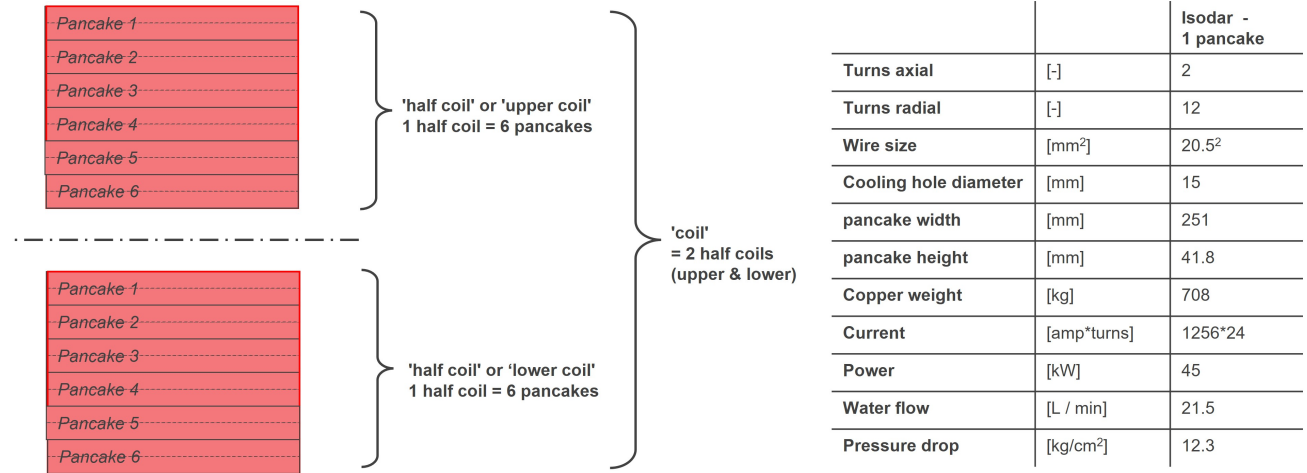


Figure 3.14: Left: schematic view of a cross-section of the main coil, with six pancakes per half coil. Right: possible configuration of the winding, using a square conductor with a round cooling channel in its center.

3.5 Coil configuration

Compared to the main coil as foreseen in the CDR, the coil height has been increased from 200 to 240 mm. Its radial width remains at 250 mm. The total current used in the calculations is of 180850 amp-turns in each of the half coils. The apparent current density is thus 3.01 A/mm², i.e. 5% lower than the 3.17 A/mm² foreseen in the CDR. This margin is taken as, at the moment, no extraction channels are foreseen in the return yoke. Including these will require to increase the main coil current.

In Fig. 3.14 a schematic view of the coil is given. Also, a possible configuration of winding and cooling is calculated. Although this configuration does not exactly sum up to a cross-section of 240 by 250 mm², it shows that a cooling configuration is feasible.

Working in pancakes gives the possibility of manufacturing the pancakes outside the cave and stacking them inside. The increase in height from 200 to 240 mm is the equivalent of adding an extra pancake.

3.6 Cyclotron RF System

Table 3.4 provides a detailed description of the RF system. The system for IsoDAR cyclotron is divided into subsystems as follows:

- The RF cavities allowing a fast acceleration to the final particle energy and keeping a large inter-turn separation. The cavities are triangular shaped and are located in the magnet valleys. There are 4 accelerating electrodes (Dees).
- The RF tuning system that will compensate for thermal drift of cavities and maintain a stable resonating frequency.
- The RF amplifiers that provide the necessary power to create the required RF electric field inside the cavity and the power to accelerate the beam.
- The RF couplers that inject the RF power from the amplifiers into the cavities
- The Low Level RF system (LLRF) that controls and regulates the RF amplitude on the Dee and drives the tuning system.

We consider these in the Sections below.

Table 3.4: Details of the RF design.

RF System Component	Design Value
Resonance Frequency	32.8 MHz
Dee voltage in the central region	70 kV
Dee voltage at extraction radius	230 kV
Dee radial extension	2 m
Dee angular extension	38°
Cavity height	1800 mm
Number of Dee stems	4 per Dee (2 up, 2 down)
Number of Dee's	4
Acceleration harmonic	4th
Power dissipated per cavity	116 kW
Cavity Q-factor	9620

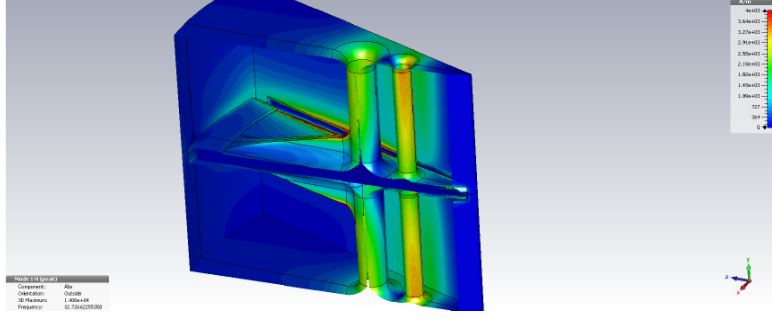


Figure 3.15: Early RF Dee computation – color scheme represent current density

3.7 RF Cavities (Dees, Stems and Liners)

The RF cavities of the cyclotron have been calculated using CST microwave studio [43] in order to define the shape of the Dee and the Dee stems. They have then been optimized also with CST from this early design. The optimization work is intended to reach the right resonance frequency, the Dee voltage Law, together with the minimal power dissipation and hence the highest quality factor (Q-factor). The field maps allow also the calculation of the couplers and voltage pick-up but this last calculation is yet to be performed.

The Dees and cavity walls are all made of OFHC copper that combines good electrical conductivity and good solder ability. The Dees are fabricated out of a 20 mm thick copper plate and are made rigid by a supporting arm. The four round stems support the Dee and provide the right inductance in order to get the required resonance frequency. Their size and location allow reaching the required Dee voltage profile versus radius. Each Dee will be equipped with vacuum pumping panels to efficiently pump the median plane. One Dee is equipped with one electrostatic deflector for extraction. This fact has not been taken into account in detail in the RF simulations to date, but some room for housing the deflector has been provisioned at the back of the Dee.

3.7.1 Integration of preliminary central region in RF Cavities

In order to compute a more accurate voltage radial dependency law, we have integrated the central region design proposed by AIMA into the RF cavity modelling, several technical choices were made to ensure the effective implementation of this innovative configuration:

- The central region 3D model was limited to 200 mm from centre.
- Both the Dee and counter dee original central region was removed by trimming the cavities at 800 mm from centre.

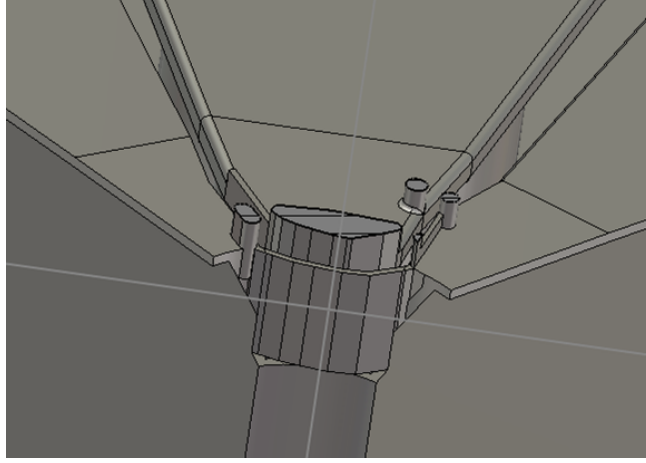


Figure 3.16: dee at central region close view

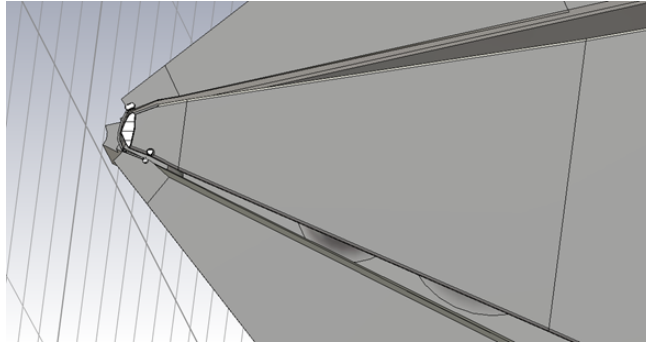


Figure 3.17: dee lofted transition top view

- Sections were cut straight, and a linear transition (loft) technique was used to achieve the connections between the trimmed components.

These lofted transition leads to an acceptable linear vertical gap opening from 26 mm at a radius of 200 mm, to 50 mm at a radius of 800 mm. In addition, adequate clearance provisions were incorporated, specifically to fit the inflector and optics coil. Symmetry with regards median plane symmetry was maintained. Power bridges between dees in the central regions were removed since we recommend to power the 4 cavities independently.

3.7.2 RFQ Integration in RF Cavities

Some clearance provision has been set for the integration of the RFQ, as seen on figure 3.19

- Diameter 280 mm
- Down to 35 cm of median plane

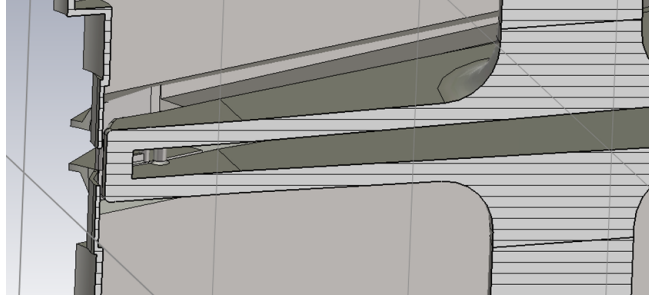


Figure 3.18: vertical gap evolution close view

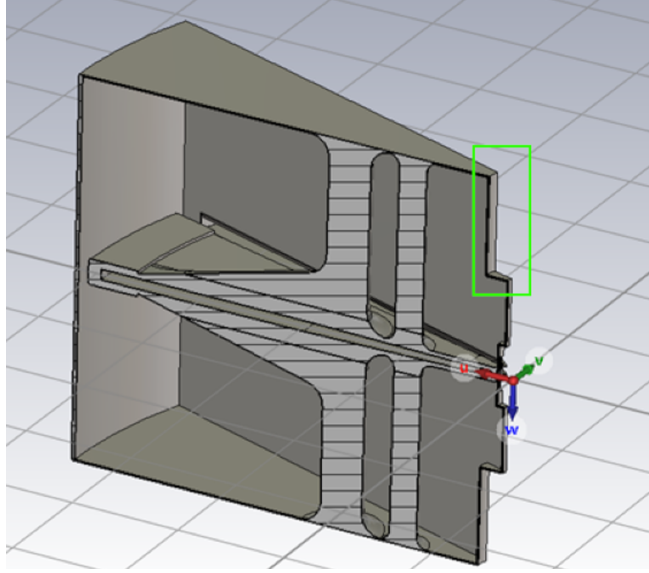


Figure 3.19: Clearance for RFQ

While the RFQ will only be in the upper location, we have decided to keep median plane symmetry, for computation, manufacturing, and performances purposes. We have observed that the RFQ clearance has a low impact on cavity frequency and performances, and the output of the RFQ could be lowered more without impacting the cavity behavior.

3.7.3 RFQ getter pumps in RF Cavities

Mastering the quality of the high vacuum is key to the success of high-power beam cyclotrons. Incorporating getter pumps in the dees, in the case of IsoDAR, would allow to enhance vacuum quality. By integrating three housing for SAES UHV1400 getter pumps per dee, we aim to ensure highly efficient and reliable vacuum performance within the Cyclotron system. The use of six of those getter pumps per cavity facilitates the effective removal of residual gases, since achieving and maintaining ultra-high vacuum conditions essential for optimal particle acceleration. Furthermore, our preliminary assessments suggest that it may be feasible to scale

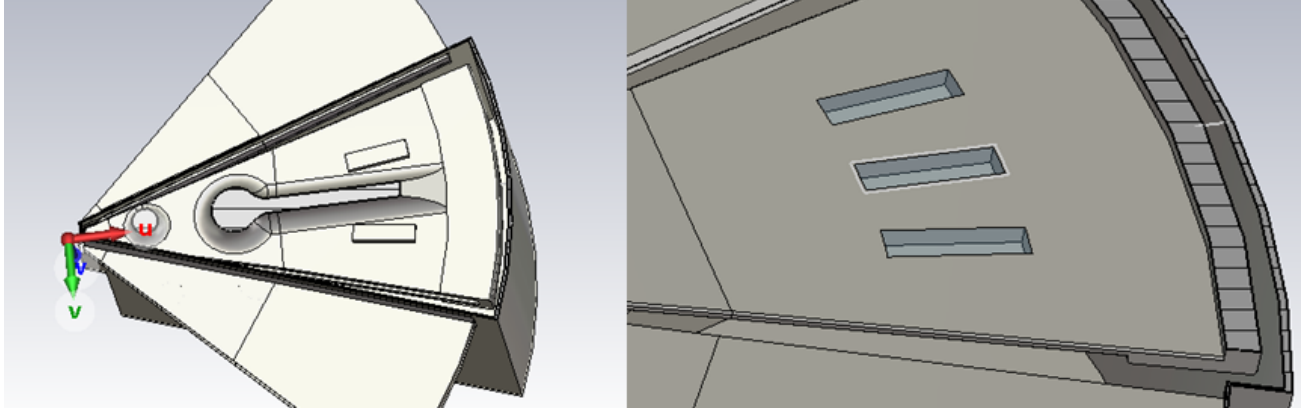


Figure 3.20: Provisional getter housings

up the configuration to include up to two sets of five getter pumps per cavity. The very low electrical field of the locations of the housings will allow the getter pumps to function safely.

This early integration of the housings of the getters in the dees is mandatory to assess their impact on the cavity frequency, and on surfaces currents. However, to finalize this integration, comprehensive vacuum computations will be needed. These computations will enable us to determine the ideal amount of getter pumps, ensuring a properly engineered vacuum system that underpins the overall success and efficiency of the Cyclotron.

3.7.4 RF Cavities design optimization

3.7.4.1 Performance requirement target

We have optimized the cavity geometry to ensure the following requirements:

- RF frequency of accelerating mode: 32.8 MHz
- Reference accelerating voltages: 70 kV @ 110 mm, 230 kV @ 2000 mm

The initial target value for the outer radius voltage was initially set at 250 kV, but according to our expertise, such high voltage will be very difficult to stand in cyclotron accelerator gaps of this size. It has been decided to reduce the target to 230 kV which remains a challenging value.

3.7.4.2 Parametric optimization of the design

We have intensively used parameters while building the CST model, to allow fast design exploration. We have retained four parameters to play with, for optimizing the cavity behavior. The

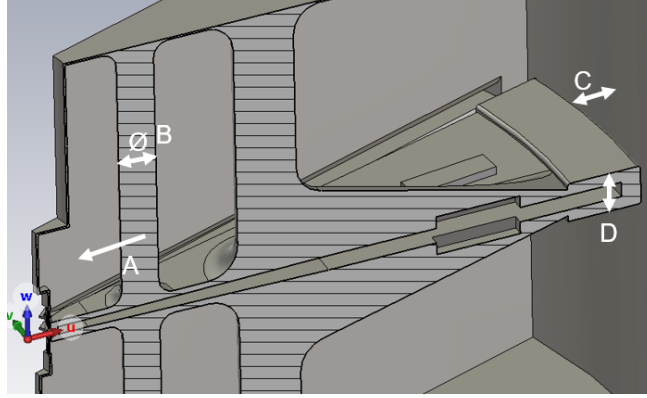


Figure 3.21: design optimization parameters

parameters, shown at figure 3.21, are defined as a deviation from the early cavity design values.

- A: 1st pillar radial position
- B: 1st pillar diameter
- C: Deflector wall distance
- D: Deflector height

CST studio suite offers an efficient optimization tools set. After some initial exploration of the values of the above-mentioned design parameters, we have optimized them using the CST optimizer.

We selected the trust region algorithm and have defined scaled goals that would ensure convergence toward the required frequency and voltages. The trust region algorithm converged in a few tens of iterations. The definition of the optimization goals, and their target and reached values are contained in table 3.5. The table 3.6 shows the optimal values reached by the optimizer.

3.7.5 RF cavity computation results

Table 3.5: RF cavities optimization goals definition and achieved values.

Goal description	Target	Final Value
Ratio between voltage at 110 mm and 2000mm	0.304348	0.303991
Model frequency divided by 32.8MHz	1	0.999871

The RF cavity computation employing the eigen mode solver on the optimized geometry yielded the following performance and characteristics of the cyclotron system:

- **Frequency:** The RF cavity operates at a frequency of 32.796 MHz, ensuring compatibility with the designed acceleration, and the RFQ integration,
- **Voltage Ratio (center to outer radius):** The reached voltage ratio is 0.303991, indicating that computed voltages at center would be 69.9 kV for a chosen voltage of 230 kV at the outer radius (2m),
- **Quality Factor (Q):** 9617,
- **Stored Energy (for max RF of 230 kV at 2 m):** 3.8 Joules
- **CST Computed Losses:** The computed losses per cavity using CST simulations are 81.3 kW,
- **Estimated Power Dissipation:** By experience, senior RF designers at IBA state that the CST eigenmode simulations underestimate the actual losses by up to 30%. If we increase the CST computed losses (81.3 kW) by this percentage, the actual estimated power dissipation per cavity becomes 116.2 kW.
- **Estimated Power Requirement:** To effectively drive the Cyclotron, each cavity will require an estimated power input of at least 266.2 kW, which include power dissipation and beam loading.
- **Maximal Surface Current:** The maximal surface current reaches 24324.6 A/m in some reduced locations. Which leads to a maximum surface power of 88.4 W/cm². This maximal surface power is localized on the dee edges. Careful attention will be required for thermal management in these regions. For the rest of the surfaces, the thermal dissipation is well below 10 W/cm². See figure 3.26 and 3.27 While matching the requirement, these computation results provide valuable information for next steps of the Cyclotron's RF cavity design including consideration in managing thermal effects.

Some illustrations of the electrical and magnetic fields computed by CST are given for reference at figures 3.22, 3.23, 3.24 and 3.25.

Table 3.6: RF cavities optimized design parameters.

Parameter	Value [mm]	Description
Deflector offset (D)	5.67	Offset of upper and lower face of deflector
Increase_diameter (B)	-3.81	Change of diameter of the pillar
Move_pillar (A)	-124.1	Radial displacement of the pillar
Back_face_offset (C)	4	Outward move of the back of the deflector

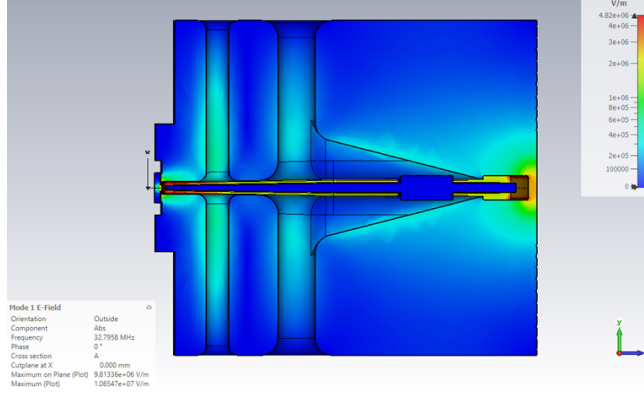


Figure 3.22: E field Vertical cross section

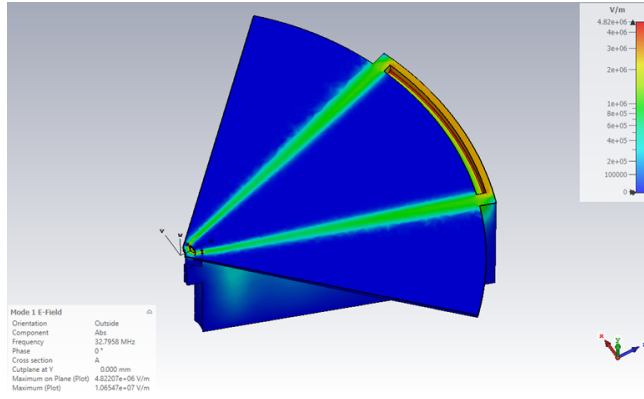


Figure 3.23: E-field Horizontal cross section

3.7.5.1 Detailed power analysis

We will now detail the post treatment of the CST results that lead to the results presented in Sec. 3.7.5. The CST eigenmode solver results are computed for a given reference energy in the system (about 1J). They must then be scaled accordingly, to reach the expected voltage at a reference location. In our case, the reference location, is the orbit at 2m, and the desired voltage is 230 kV.

The ratio of the desired voltage to the reference voltage at 2m is 1.947. We can scale the currents and voltages using this factor. We can also scale the energies, power and losses using this factor squared (formulae 3.1, 3.2 and 3.3). We thus have:

$$E_{stored} = E_{stored,ref} \frac{V_{target}^2}{V_{ref}^2} \quad (3.1)$$

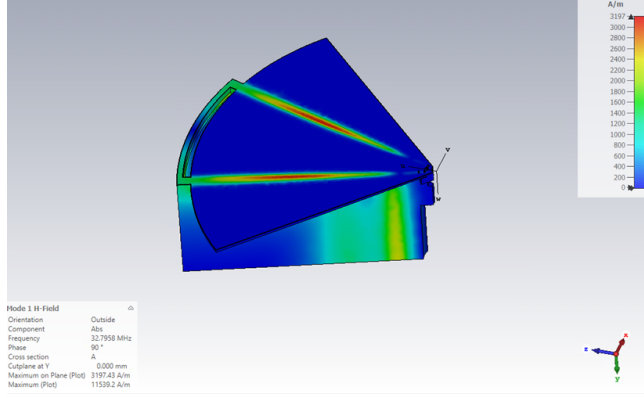


Figure 3.24: H-field horizontal cross section

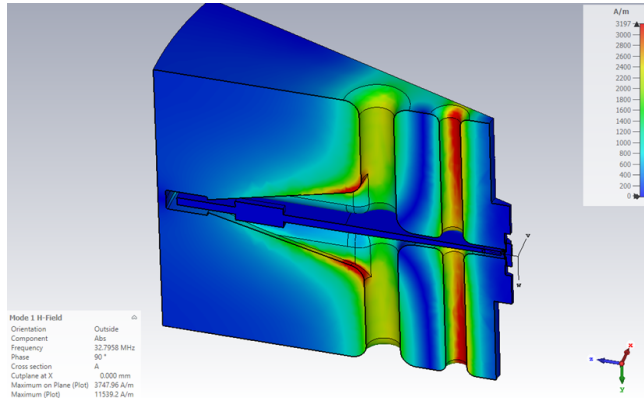


Figure 3.25: H-field vertical cross section

$$P_{loss} = P_{loss,ref} \frac{V_{target}^2}{V_{ref}^2} \quad (3.2)$$

$$I_s = I_{s,ref} \frac{V_{target}}{V_{ref}} \quad (3.3)$$

CST provides the maximal surface current I_s in the cavity which isn't a directly useful value, but we can compute from it the maximal surface power dissipation P_s , which will be useful for designing the cooling system sizing and layout. We first need to compute the surface resistance R_s whose formula, given above uses the conductivity σ and the RF skin depth δ (see formulae 3.4, 3.5 and 3.6). we end up with a maximal surface dissipation Power 88.4 W/cm². This value, despite being high, only concerns the very small surface of the dee edges, and should not be considered as an issue for the design of the cooling system.

$$R_s = \frac{1}{\sigma \cdot \delta} \quad (3.4)$$

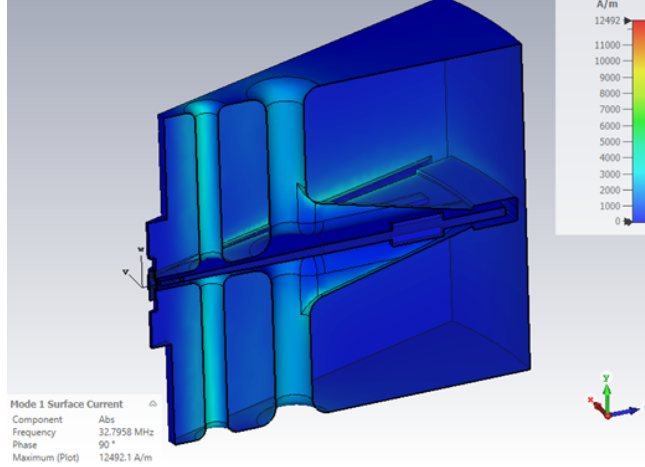


Figure 3.26: Surface currents

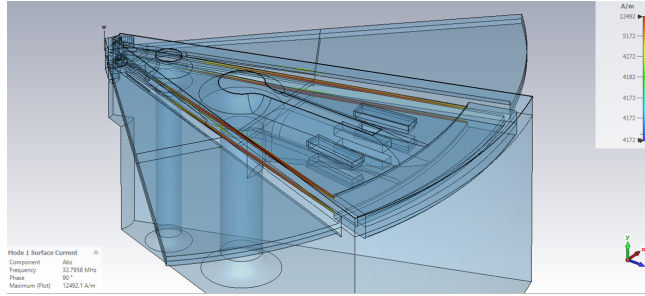


Figure 3.27: Surface current generating more than 10 W/cm²

$$\delta = \sqrt{\frac{2}{\sigma \cdot \mu \cdot \omega}} \quad (3.5)$$

$$P_s = R_s I_s^2 \quad (3.6)$$

3.7.5.2 Radial voltage dependency

The voltages at different radii have been calculated by integrating the electrical field along circular arcs crossing the acceleration gaps, and reference curves crossing central gap and the dee outer edge gap. The transit time factor has not been considered. The computed voltages have then been scaled to match a target voltage of 230 kV at 2 m. The resulting absolute and normalized voltage radial dependency are given in figure 3.28 and table 3.9

Table 3.7: Optimized cavities, functional characteristics

	CST reference	Scaled value
Stored energy [J]	1.001	3.796
Voltage at on the 2m orbit [kV]	118.12	230
Voltage at center [kV]	35.91	69.9
Maximal voltage at outer edge of the dee [kV]	126.55	246.4
Computed losses [kW]	21.452	81.3
Maximal surface current [A/m]	12492.1	24324.6

Table 3.8: Cavity properties for computing surface dissipation

Property	Value
Copper magnetic permeability μ	$0.99991 \times 4\pi \times 10^{-7}$ H/m
Copper conductivity σ	5.8×10^7 S/m
Angular Frequency ω	$2\pi \times 32.796 \times 10^6$ rad/s
Skin Depth δ	11.53 μ m

3.7.6 RF Tuning System

The tuning system is a movable plate or loop that corrects the resonance frequency drift mainly caused by RF heating. The system here is based on four separated tuning plates (one per cavity) and located in the median plane. The plate is accurately displaced by an electrical motor via a ball screw. Similar systems are already used many commercial cyclotrons.

3.7.7 RF Amplifiers

Traditionally a large part of the cyclotron RF budget is dedicated to the RF power source. This is especially true for this cyclotron, as it requires a high Dee voltage and accelerates 600 kW of beam power. This means that the total RF power exceeds 1 MW. Here we assume 1200 kW of RF power, which corresponds to a 50% efficiency of RF power to beam power. Since the four cavities are driven separately we are speaking about 4 distinct amplifier chains of 300 kW each.

The traditional way to produce such a high RF power is still today the use of vacuum tubes (triodes or tetrodes) and this is especially true in the accelerator world where the load constraints are more severe than simple antennas. On the other hand solid state technology made a significant step forward in the past years in terms of power density and robustness. Even though the last generation of LDMOS allows to make solid state amplifiers at nearly competitive price with respect to vacuum tubes and that are also very reliable, we do believe vacuum tubes still present reliability and maintainability advantages for powering the isoDAR cyclotron, given the harsh environment where those amplifiers will be located. Tubes amplifiers will also accommodate

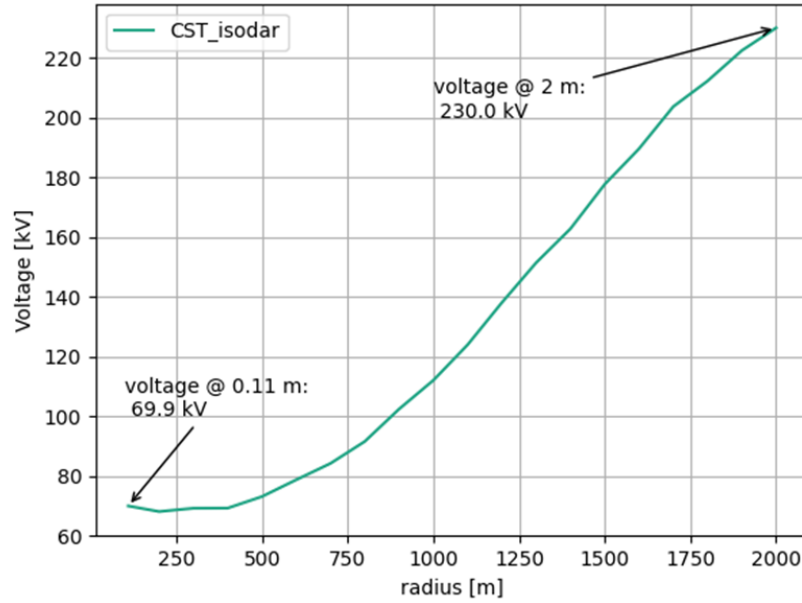


Figure 3.28: Dee voltage radial dependency

easily to the rapid variations of load due to beam temporal pattern.

3.7.8 RF Lines and Couplers

The RF power is fed to the cavities through EIA 6 1/8" solid copper coax line. There are basically two ways to couple RF to the cavities:

- Capacitively in the median plane
- Inductively in the bottom (or top) of the cavity liner.

The choice between these two alternatives is mainly driven by the available space, the field patterns and the cooling concerns. The usual experience in this field is that both systems can work and couplers up to 800 kW at 107 MHz have been successfully built and operated.

Four couplers are needed for the complete cyclotron. The 300 kW power will be injected via one coupler per cavity.

Eventhough capacitive coupling might be less prone to multipacting by the fact that the coupling antenna could be easily DC biased, our expertise in high power coupler design advocates for an inductive solution. The design of inductive coupler being easier to watercool, and there is

Table 3.9: RF voltage radial dependency.

Radius [mm]	Voltage [kV]
center	69.9
110	69.918
200	68.04
300	69.149
400	69.187
500	73.054
600	78.677
700	84.162
800	91.511
900	102.353
1000	111.984
1100	123.881
1200	138.013
1300	151.364
1400	162.731
1500	177.622
1600	189.519
1700	203.636
1800	212.224
1900	222.408
2000	230
Outer radius	246.4

a wide area where H-field is high enough for efficient coupling behind the second pillar of the cavity.

We have initiated a preliminary design computation of such a inductance coupler, feeding the RF power from a EIA 6"1/8 port. The suggested design is a loop made out of a 20x60 mm rectangular section bar, offering room for water-cooling. See figure 3.29. The adaptation tuning will be performed by rotation of the loop around the vertical axis. The design has been optimized with a default angle of 45° to the cavity axis, in order to allow a maximal tuning range.

The optimization of the coupler loop, for a cavity loaded with 150 kW of beam leads to an height of 362 mm, wich provides a good matching (figure 3.30) and a $S_{1,1}$ scattering parameter inferior to 0.01.

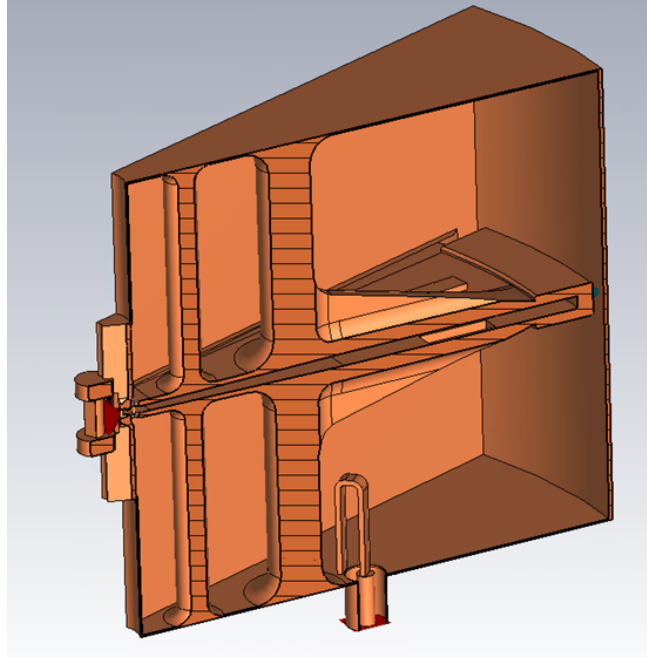


Figure 3.29: RF loop coupler design

3.7.9 LLRF Electronics

The LLRF (Low Level RF) controls the RF amplitude and phase of the signal sent to the amplifiers. It also controls the tuning mechanism in order to maintain constant resonant frequencies in the cavities. The amplitude and phase control is based on feed-back signals coming from the cavities and amplifiers. In order to avoid the multipactor effect the LLRF manages also a pulsing mode that provides for an easy start-up and reduces the power dissipated in the amplifiers. One LLRF system per cavity is planned.

An additional electronic element is needed to keep a stable phase difference between the different cavities.

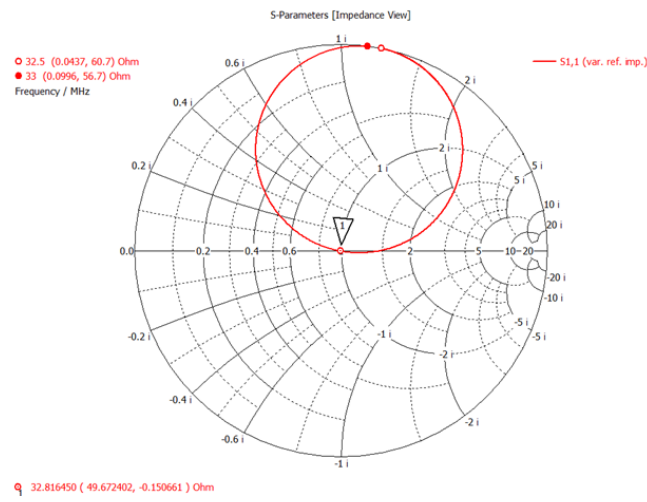


Figure 3.30: Coupler port impedance

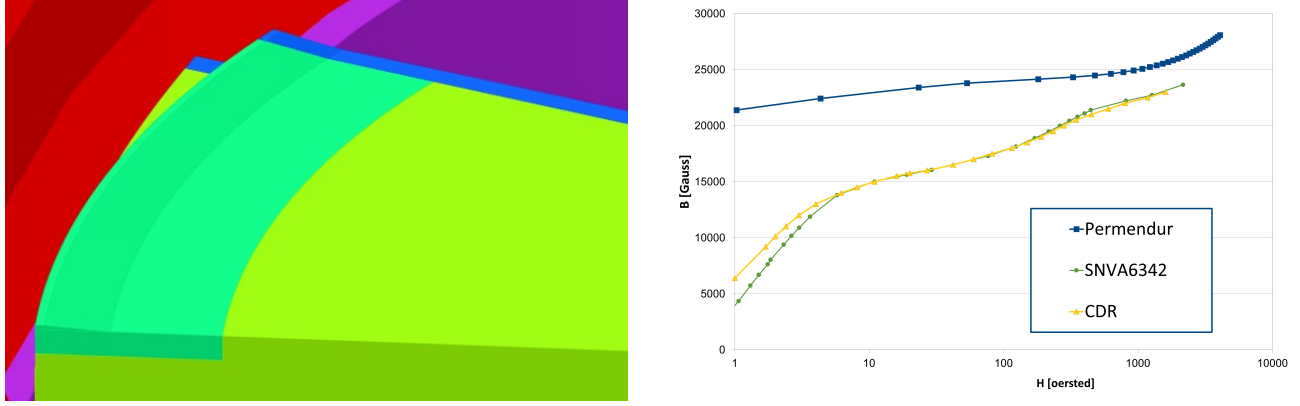


Figure 3.31: Left: Detailed view of the outer radius of the pole; only half of one pole is shown. In red is the coil, in light green is the pole made of SNVA6342 steel. The turquoise part is a piece 30 mm in height and 200 mm in width made of permendur. In blue we see the pole edge made of SNVA6342 steel, which can be shimmed to isochronize the magnetic field. Right: BH curves for the two steel types used: Permendur and SNVA6342. As reference, the BH curve used for the cyclotron in the CDR is also shown.

3.8 Cyclotron magnetic performance

In this section we describe the latest modifications applied to the cyclotron regarding its magnetic properties. We will compare the results with the model from the Conceptual Design Report (CDR) from [6] to ensure its magnetic performance remain within specifications.

With the latest design of the vacuum chamber, see section 3.4, the pole radius was slightly reduced. To keep the magnetic field isochronous up to extraction at 120 MeV, the outer radius was therefore somewhat modified, see left image in Fig. 3.31. First, the curvature was modified to follow the curvature of the last orbit. This enhances the total flux in the region where needed. Second, the top layer of the pole at its outer radius will be made of permendur. This alloy has better magnetic properties at high field, and enhances again the magnetic flux. Finally, the pole height is increased by a slanted ridge at its extremity. This reduction of the pole gap should have no effect on the transmission and can be tuned to improve the dB/dr for the last orbits.

The steel used for the cyclotron yoke and poles is the SNVA6342, also used for example in the C400 cyclotron (see Ref. [44]). Its BH-curve is shown in fig 3.31. Here, we also see the better performance of the permendur alloy.

3.8.1 Isochronization

The edge of the pole can be shimmed to isochronize the magnetic field map. In Fig. 3.32 the latest results are given. The left image shows the shimming applied, the right image shows

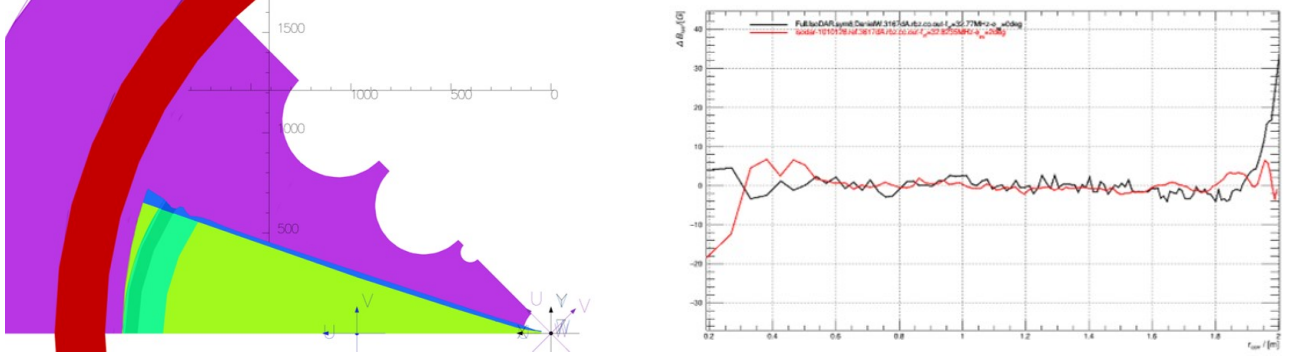


Figure 3.32: Left: Pole edge of isochronized model. Right: the dB [Gauss] as a function of radius [meters], for the CDR model (in black) and the newest model (in red). Note that a positive dB means there is too little field at specific radius, a negative dB implies there is too much field. The RF-frequency for the CDR model is at 32.77 MHz, for the newest model it is 32.82 MHz.

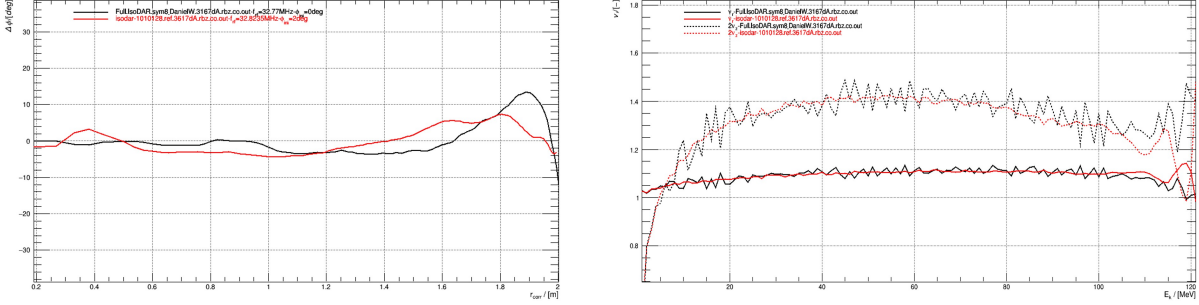


Figure 3.33: Left: phase slip as a function of radius. Right: vertical and horizontal tunes as a function of energy (dashed and solid lines respectively). Shown are the results for the CDR model (in black) and the newest model (in red).

the offset in magnetic field, as required for a given RF-frequency. For comparison, the offset (expressed as dB in Gauss) for the model of the CDR is also shown.

The plot shows that the magnetic field is stable and strong enough up to a radius of 2 meters, which is the equivalent of 121 MeV. In Fig 3.33 the phase slip can be seen to stay within the $\pm 10^\circ$. The horizontal and vertical tunes are also given in the same figure. Here we see that there is a crossing of the tunes at high radius, invoking resonances which could impact the extraction.

As a conclusion, we can state that a configuration is possible with an isochronous magnetic field for up to 121 MeV. The transition to perpendicular at high radius, together with an abrupt slanted pole face, requires shimming of the pole edge. In a further study, these last modifications can be made more smooth, as not to have too much of a fluctuation in the dB for the last orbits and thus tunes that do not cross anymore, avoiding possible resonances.

Chapter 4

Installation in the Yemilab Setting

The most likely deployment scenario is at the Yemilab underground laboratory, 1 km below the surface adjacent to the Handuk iron mine in the Republic of Korea. Fig. 4.1 schematically shows Yemilab, accessed either by a 6 km meter ramp descending 750 meters at a 15% slope from a surface access point into the mine, or by an elevator conveyance in a new 600 meter vertical shaft. Unfortunately, the elevator is suitable only for personnel access, all heavy and bulky equipment must be brought down through the ramp. Fig. 4.2 details the area where the IsoDAR experiment would be installed, with the target only a few meters from the planned 3 kiloton LSC (Liquid Scintillator Counter). Site-specific questions will be addressed in Volume III of this PDR and the following section aims at a general description of deployment strategies in an underground setting, pertaining only to the cyclotron. In this document we use Yemilab as the example, noting that most of the issues discussed will arise in an equivalent manner at other installation sites.

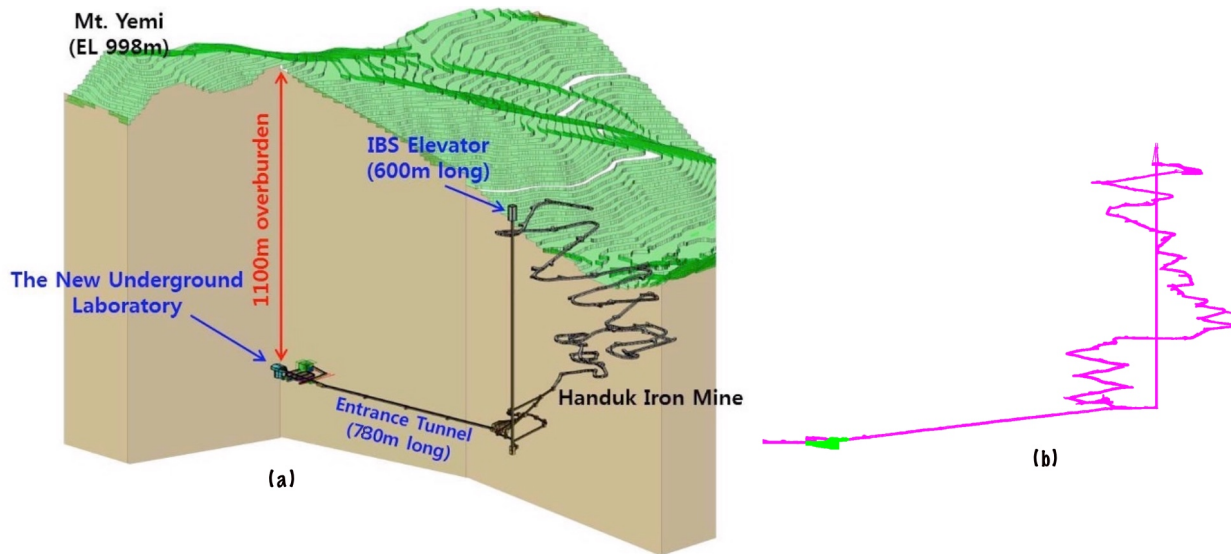


Figure 4.1: (a) Schematic of Handuk/Yemilab area, (b) Low resolution laser scan of Handuk mine and Yemilab access ramps, green area denotes high resolution scans of IsoDAR deployment area, shown in more detail in the next figure.

❖ Yemilab Layout (Top view)

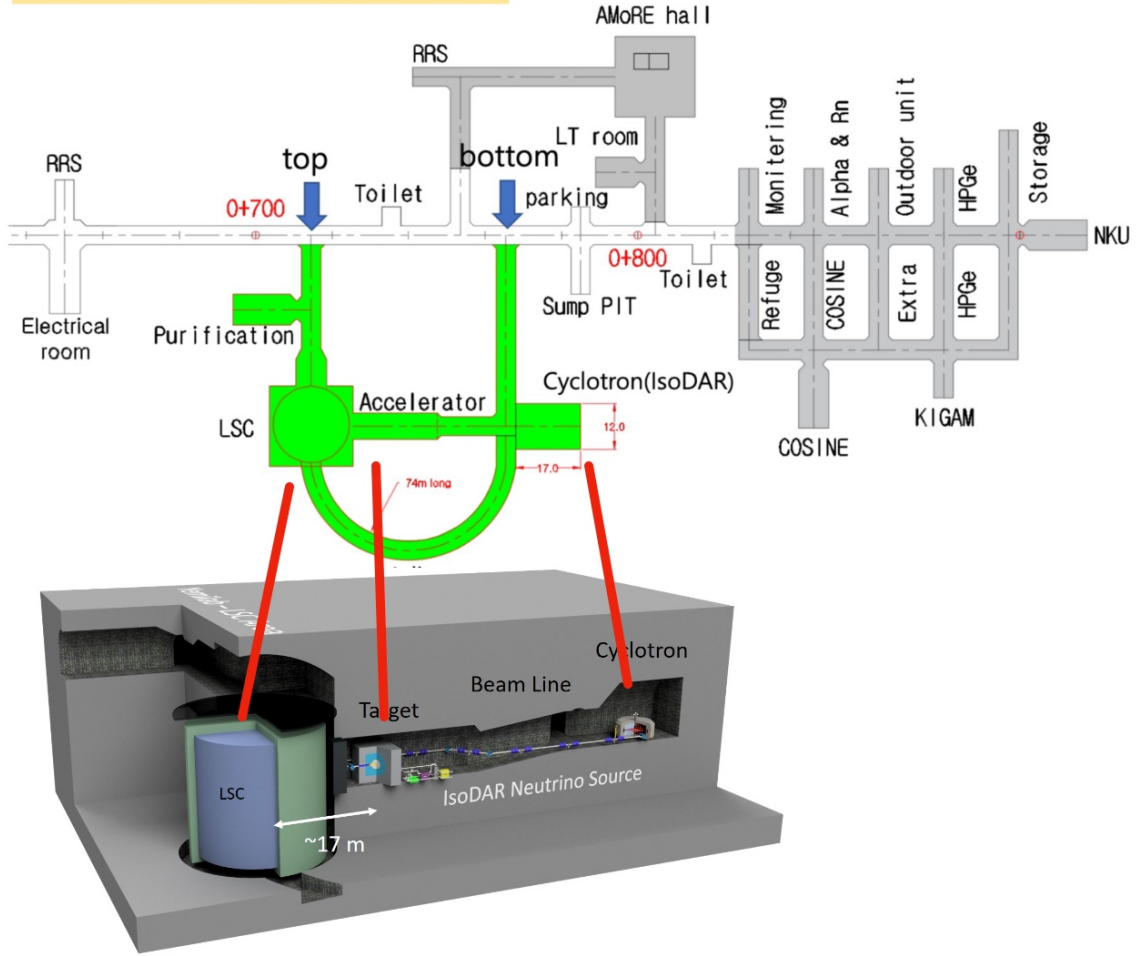


Figure 4.2: Layout of Yemilab, showing (in green) the area where IsoDAR will be installed. The cyclotron will be assembled in the dedicated cyclotron vault as shown.

4.1 Transport of Components

All of the components of the experiment must be brought to the site from the port-of-entry into the Republic of Korea. The preferred method is to use trucks along the highways. Prior experience of IBA with rail transport has been that it is difficult to provide adequate shock protection, and heavy pieces can be damaged in transit. As stated above, transport from the surface to the experimental site must be accomplished by way of the mine ramp depicted in Fig. 4.1. Nominally, its cross section is 5 x 5 meters, however we are told that pinch points and sharp bends may occur and might provide challenging areas to transport large, heavy loads through. We have received assurance that large mining trucks, 3.5 meters wide, can traverse the entire ramp, as this is the way ore was transported to the surface for many years.

While high-resolution laser scans of the IsoDAR and LSC areas have been performed, (cf. Fig-

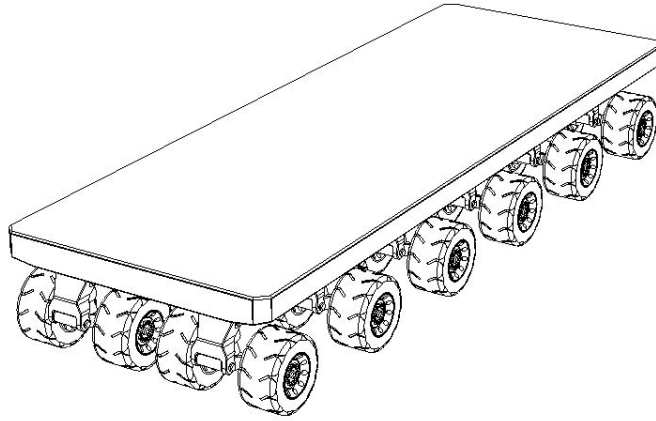


Figure 4.3: A typical SPMT vehicle, extremely versatile and capable of extremely heavy loads over irregular terrain

ures 4.8 and 4.9), the resolution of the laser scans of the access ramp areas are not of sufficient resolution to provide enough detailed information about the location or size of the possible constrictions. Improved scans must be performed as part of final installation planning, and will be included in volume III which will be site-specific to Yemilab.

As seen in the previous chapter, the iron pieces that make up the cyclotron magnet, although heavy, are not in themselves large, so the pinch points are not likely to be a problem for bringing the magnet steel to the installation site. The plan is to use an SPMT vehicle (Self-Propelled Modular Transporter) shown in Fig. 4.3 for bringing the magnet and vacuum liner pieces from the surface. These electrically-powered vehicles are flexible in their size, the sets of 4 tires are independently steerable, so the vehicle is extremely maneuverable, and can easily accommodate the heaviest piece of magnet steel [45].

The only challenge will be the magnet coils. Each of the two coil packages measures 5 meters across and 0.3 meters high, the individual coils inside measure 4.960×0.252 meters. Figs. 4.4 and 4.5 gives an approximate view of a coil package and the clearances in the access ramp to the Laboratory (marked as the "Entrance Tunnel" in Fig. 4.1 (a)). This particular ramp is well-constructed and engineered, and has a measured width of 5 meters. A special mounting fixture capable of holding the coil packages at an angle should be able to bring these coils through this particular passageway. There are constrictions even in this ramp: cable trays and service boxes, however these can be moved if necessary. Uncertainty remains as to whether this type of conveyance device for the coils can navigate the winding ramp from the surface.

In the unlikely case the individual pancakes do not fit through the constriction points, the alternative is to wind and pot the coils underground, or make them in sections. This has already been studied in Chapter 3 of the CDR document [2], [46]. The heavy winding machine and fixtures would need to be transported, but could be broken down into parts that will fit

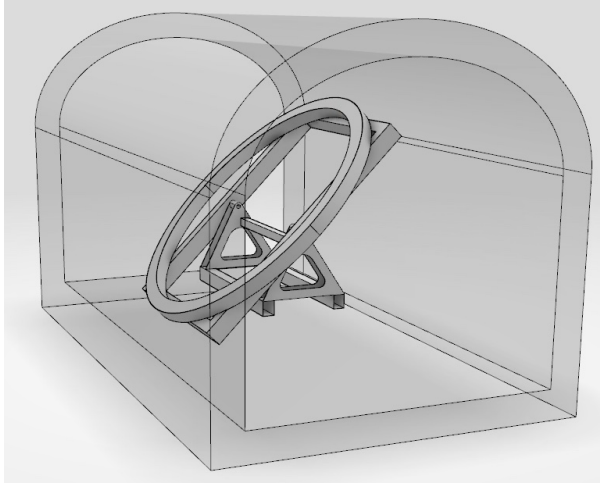


Figure 4.4: Isometric view of the coil package, on a specially-designed cart, transporting the coil through the access ramp to the Yemilab campus.

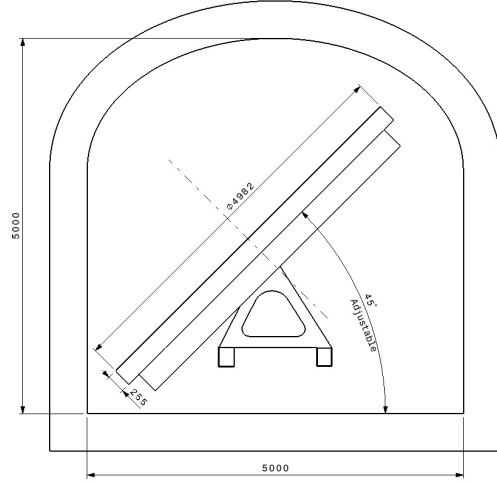


Figure 4.5: This ramp is engineered to a 5-meter width, and maximum height of 5 meters. Unfortunately we do not have sufficient information about the winding access ramp from the surface to the base of the shaft to assess at this time whether transport of the coils will be possible with this conveyance device.

through the ramps, then assembled on site. The biggest challenge would be the ventilation scheme for the potting process. There is precedence for sectioned coils. For the large TRIUMF cyclotron [47], coils are separated into six different segments as the outer diameter of the coils is almost 20 meters, making the transport of fully assembled coils essentially impossible over conventional roadways. The inconvenience for a segmented coil, is that the ends of every turn of every section must be spliced, substantially increasing the cost and decreasing the efficiency of operation, as the coil must have as few turns as possible with very high current flowing through each turn.

4.2 Assembly underground

The cyclotron will be assembled in a hall measuring 12 meters wide, 17 meters deep and 10 meters high. This hall was excavated to our specifications at the 90 degree bend in the access ramp to the LSC, as seen in Fig. 4.2. A flat area, roughly 10 m x 5 m at the corner will be the staging area for components transported from the surface. A bridge crane riding on tracks will be used to rig parts to the cyclotron assembly point. Conversations with a crane manufacturer, Industrias Electromecánicas GH, S.A. [48] gave us assurances that a 40-ton capacity crane, riding on rails installed on the cavern floor would be quite practical (see Fig. 4.6. It could be



Figure 4.6: Examples of GH gantry cranes, capacities: foreground 20 tons, background 260 tons

configured to fit the dimensions of the cavern, and broken into modular parts that could be transported to the site.

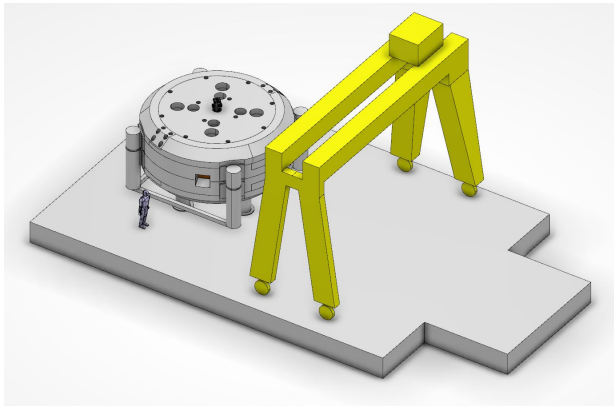


Figure 4.7: Cyclotron and crane on cavern floor.

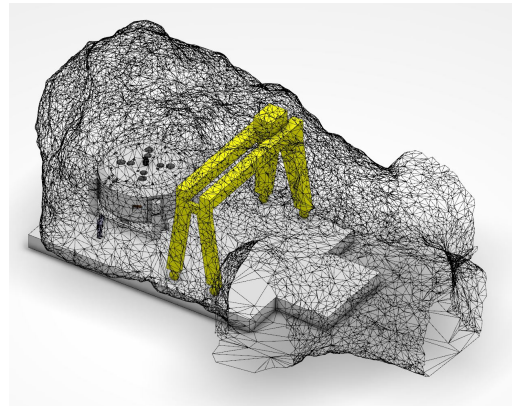


Figure 4.8: Cyclotron and crane inside the cavern.

An overview of the cyclotron inside the cavern with the rigging equipment is shown in Figures 4.7 - 4.9. It should be noted that the gantry crane will be dismantled once the heavy parts are rigged. This would increase the clearance above the cyclotron for the additional equipment. In addition, the large crane can be reconfigured and reassembled in the target hall, and used for assembly of the MEBT, target and shielding, and for subsequent maintenance of the target systems.

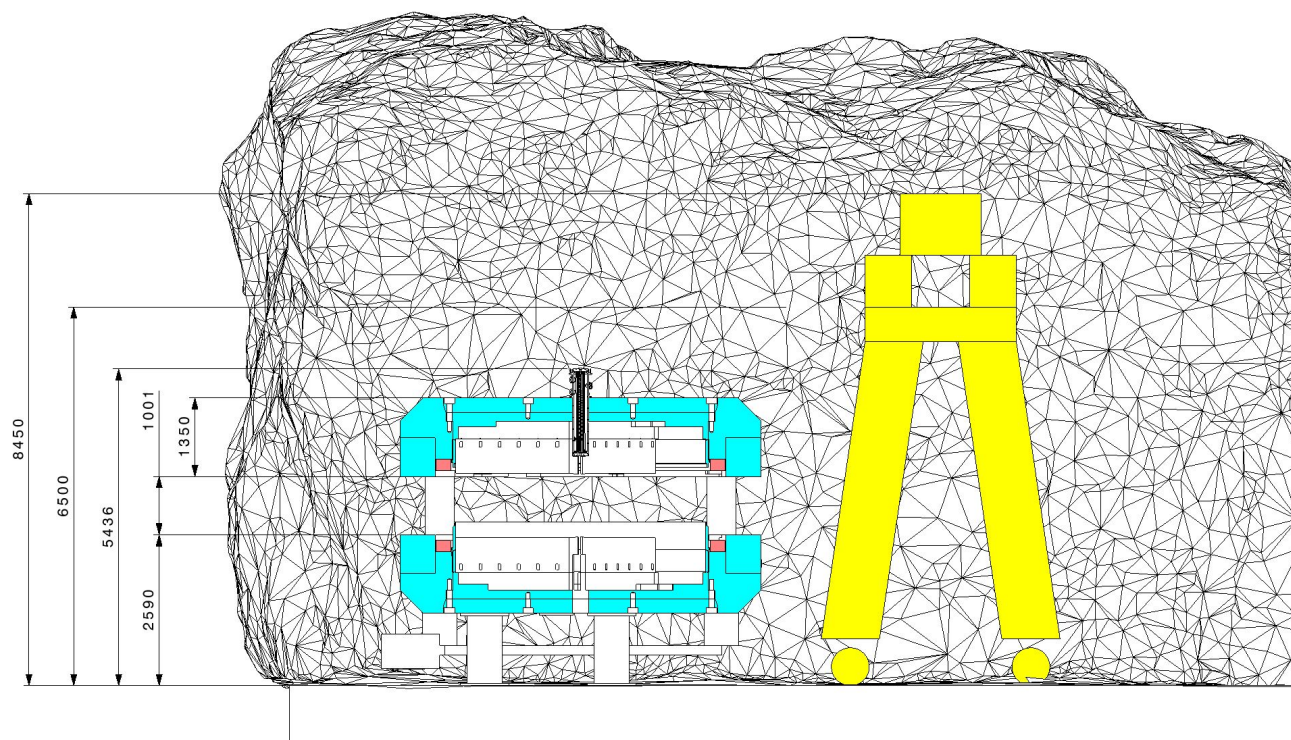


Figure 4.9: Cyclotron open and crane with cavern mesh - cut-view.

Chapter 5

Conclusion

5.1 Summary

In this version 0.9 of the document, we presented the preliminary design of the IsoDAR compact cyclotron with RFQ injection, including ion source and low energy beam transport.

The presented design study shows the feasibility of producing a high current (10 mA of protons through stripping of a 5 mA H_2^+ beam) in a compact cyclotron. It further shows a convincing strategy to segment the cyclotron yoke for transportation into the underground environment to be assembled in situ at the final location.

RF calculations show manageable power and cooling, the required radial voltage distribution in the accelerating gaps, and adequate room for vacuum getter pumps.

In a future update to this PDR document, we plan to show a full start-to-end beam dynamics study, based on the presented individual components' beam simulations. We will also add a risk assessment, and additional details on the extraction system, based on the cited publications and ongoing design work. Finally, we will include a vacuum calculation based on MolFlow.

5.2 Acknowledgements

This work was primarily supported by NSF grant PHY-2012897. Preliminary work leading up to this was supported by NSF grants PHY-1912764 and PHY-1626069. Moon was supported by DOE grant DE-SC0024138. Winklehner was supported by the Heising-Simons Foundation.

Bibliography

- [1] P. Calvo, D. Winklehner, and C. Oliver, “Analyzing beam-gas interactions in an H₂ + cyclotron beam,” en, *Journal of Physics G: Nuclear and Particle Physics*, 2023, ISSN: 0954-3899. DOI: 10.1088/1361-6471/acfe8f. [Online]. Available: <http://iopscience.iop.org/article/10.1088/1361-6471/acfe8f> (visited on 10/11/2023).
- [2] J. R. Alonso, J. M. Conrad, D. Winklehner, *et al.*, “IsoDAR@Yemilab: A report on the technology, capabilities, and deployment,” en, *Journal of Instrumentation*, vol. 17, no. 09, P09042, Sep. 2022, Publisher: IOP Publishing, ISSN: 1748-0221. DOI: 10.1088/1748-0221/17/09/P09042. [Online]. Available: <https://doi.org/10.1088/1748-0221/17/09/p09042> (visited on 09/30/2022).
- [3] S.-H. Seo, J. Alonso, P. Bakhti, *et al.*, *Physics Potential of a Few Kiloton Scale Neutrino Detector at a Deep Underground Lab in Korea*, arXiv:2309.13435 [hep-ex, physics:hep-ph], Sep. 2023. DOI: 10.48550/arXiv.2309.13435. [Online]. Available: <http://arxiv.org/abs/2309.13435> (visited on 10/11/2023).
- [4] J. Alonso, C. A. Argüelles, A. Bungau, *et al.*, “Neutrino physics opportunities with the IsoDAR source at Yemilab,” *Physical Review D*, vol. 105, no. 5, p. 052009, Mar. 2022, Publisher: American Physical Society. DOI: 10.1103/PhysRevD.105.052009. [Online]. Available: <https://link.aps.org/doi/10.1103/PhysRevD.105.052009> (visited on 05/31/2022).
- [5] L. Waites, A. Thompson, A. Bungau, *et al.*, “Axionlike particle production at beam dump experiments with distinct nuclear excitation lines,” *Physical Review D*, vol. 107, no. 9, p. 095010, May 2023, Publisher: American Physical Society. DOI: 10.1103/PhysRevD.107.095010. [Online]. Available: <https://link.aps.org/doi/10.1103/PhysRevD.107.095010> (visited on 05/11/2023).
- [6] M. Abs, A. Adelmann, J. R. Alonso, *et al.*, *IsoDAR@KamLAND: A Conceptual Design Report for the Technical Facility*, arXiv: 1511.05130, Nov. 2015. [Online]. Available: <http://arxiv.org/abs/1511.05130> (visited on 05/06/2020).
- [7] J. Stetson, S. Adam, M. Humbel, *et al.*, “The commissioning of PSI injector 2 for high intensity, high quality beams,” in *13th International Conference on Cyclotrons and their Applications*, 1992, p. 4.
- [8] C. Baumgarten, “Transverse-longitudinal coupling by space charge in cyclotrons,” *Physical Review Special Topics-Accelerators and Beams*, vol. 14, no. 11, p. 114201, 2011.
- [9] D. Winklehner, J. M. Conrad, D. Schoen, *et al.*, “Order-of-magnitude beam current improvement in compact cyclotrons,” en, *New Journal of Physics*, vol. 24, no. 2, p. 023038, Feb. 2022, Publisher: IOP Publishing, ISSN: 1367-2630. DOI: 10.1088/1367-2630/ac5001. [Online]. Available: <https://doi.org/10.1088/1367-2630/ac5001> (visited on 03/07/2022).

- [10] D. Winklehner, J. Bahng, L. Calabretta, *et al.*, “High intensity cyclotrons for neutrino physics,” *Nuclear Instruments and Methods in Physics Research Section A: Accelerators, Spectrometers, Detectors and Associated Equipment*, Advances in Instrumentation and Experimental Methods (Special Issue in Honour of Cai Siegbahn), vol. 907, pp. 231–243, Nov. 2018, ISSN: 0168-9002. DOI: 10.1016/j.nima.2018.07.036. [Online]. Available: <http://www.sciencedirect.com/science/article/pii/S0168900218308714> (visited on 10/04/2018).
- [11] M. Hostert, D. McKeen, M. Pospelov, *et al.*, “Dark sectors in neutron-shining-through-a-wall and nuclear absorption signals,” Jan. 2022. arXiv: 2201.02603 [hep-ph].
- [12] A. Bungau, J. Alonso, L. Bartoszek, *et al.*, “Optimizing the ^8Li yield for the IsoDAR Neutrino Experiment,” in, *Journal of Instrumentation*, vol. 14, no. 03, P03001–P03001, Mar. 2019, Publisher: IOP Publishing, ISSN: 1748-0221. DOI: 10.1088/1748-0221/14/03/P03001. [Online]. Available: <https://iopscience.iop.org/article/10.1088/1748-0221/14/03/P03001> (visited on 08/18/2020).
- [13] A. Bungau, J. Alonso, L. Bartoszek, *et al.*, “The shielding design concept for the ISODAR neutrino target,” in, *Journal of Instrumentation*, vol. 15, no. 07, T07002–T07002, Jul. 2020, Publisher: IOP Publishing, ISSN: 1748-0221. DOI: 10.1088/1748-0221/15/07/T07002. [Online]. Available: <https://iopscience.iop.org/article/10.1088/1748-0221/15/07/T07002> (visited on 08/18/2020).
- [14] J. M. Hardin, I. Martinez-Soler, A. Diaz, *et al.*, “New Clues about light sterile neutrinos: preference for models with damping effects in global fits,” *JHEP*, vol. 09, p. 058, 2023. DOI: 10.1007/JHEP09(2023)058. arXiv: 2211.02610 [hep-ph].
- [15] G. Karagiorgi, B. R. Littlejohn, P. Machado, *et al.*, “Snowmass Neutrino Frontier: NF02 Topical Group Report on Understanding Experimental Neutrino Anomalies,” in *2022 Snowmass Summer Study*, Sep. 2022. arXiv: 2209.05352 [hep-ex].
- [16] A. Diaz, C. A. Argüelles, G. H. Collin, *et al.*, “Where Are We With Light Sterile Neutrinos?” *Phys. Rept.*, vol. 884, pp. 1–59, 2020. DOI: 10.1016/j.physrep.2020.08.005. arXiv: 1906.00045 [hep-ex].
- [17] M. D. J.S. Nico, D. Gilliam, F. E. Wietfeldt, *et al.*, “Measurement of the neutron lifetime by counting trapped protons in a cold neutron beam,” *Phys. Rev. C*, vol. 71, p. 055 502, 2005. DOI: 10.1103/PhysRevC.71.055502. arXiv: nucl-ex/0411041.
- [18] A. T. Yue, M. S. Dewey, D. M. Gilliam, *et al.*, “Improved Determination of the Neutron Lifetime,” *Phys. Rev. Lett.*, vol. 111, no. 22, p. 222 501, 2013. DOI: 10.1103/PhysRevLett.111.222501. arXiv: 1309.2623 [nucl-ex].
- [19] A. P. Serebrov, E. . Kolomensky, A. K. Fomin, *et al.*, “Neutron lifetime measurements with a large gravitational trap for ultracold neutrons,” *Phys. Rev. C*, vol. 97, no. 5, p. 055 503, 2018. DOI: 10.1103/PhysRevC.97.055503. arXiv: 1712.05663 [nucl-ex].
- [20] F. M. Gonzalez *et al.*, “Improved Neutron Lifetime Measurement with UCN τ ,” *Phys. Rev. Lett.*, vol. 127, no. 16, p. 162 501, 2021. DOI: 10.1103/PhysRevLett.127.162501. arXiv: 2106.10375 [nucl-ex].

- [21] Z. Berezhiani, “A possible shortcut for neutron–antineutron oscillation through mirror world,” *Eur. Phys. J. C*, vol. 81, no. 1, p. 33, 2021. DOI: 10.1140/epjc/s10052-020-08824-9. arXiv: 2002.05609 [hep-ph].
- [22] P. A. Zyla *et al.*, “Review of Particle Physics,” *PTEP*, vol. 2020, no. 8, p. 083C01, 2020. DOI: 10.1093/ptep/ptaa104.
- [23] D. V. Forero and M. M. Guzzo, “Constraining nonstandard neutrino interactions with electrons,” *Phys. Rev. D*, vol. 84, p. 013002, 1 Jul. 2011. DOI: 10.1103/PhysRevD.84.013002. [Online]. Available: <https://link.aps.org/doi/10.1103/PhysRevD.84.013002>.
- [24] T. Stambach, S. Adam, T. Blumer, *et al.*, “The PSI 2mA beam and future applications,” *AIP Conference Proceedings*, vol. 600, no. 1, pp. 423–427, Dec. 2001, ISSN: 0094-243X. DOI: 10.1063/1.1435294. eprint: https://pubs.aip.org/aip/acp/article-pdf/600/1/423/12144003/423_1_online.pdf. [Online]. Available: <https://doi.org/10.1063/1.1435294>.
- [25] S. Axani, D. Winklehner, J. Alonso, *et al.*, “A high intensity H₂⁺ multicusp ion source for the isotope decay-at-rest experiment, IsoDAR,” *Review of Scientific Instruments*, vol. 87, no. 2, 02B704, Oct. 2015, Publisher: American Institute of Physics, ISSN: 0034-6748. DOI: 10.1063/1.4932395. [Online]. Available: <https://aip.scitation.org/doi/10.1063/1.4932395> (visited on 03/04/2021).
- [26] D. Winklehner, S. Axani, P. Bedard, *et al.*, “First commissioning results of the multicusp ion source at MIT (MIST-1) for H₂⁺,” in *AIP Conference Proceedings*, vol. 2011, American Institute of Physics, Sep. 2018, p. 030002. DOI: 10.1063/1.5053263. [Online]. Available: <https://aip.scitation.org/doi/abs/10.1063/1.5053263> (visited on 10/11/2022).
- [27] D. Winklehner, J. M. Conrad, J. Smolsky, *et al.*, “High-current H₂⁺ beams from a filament-driven multicusp ion source,” *Review of Scientific Instruments*, vol. 92, no. 12, p. 123301, Dec. 2021, Publisher: American Institute of Physics, ISSN: 0034-6748. DOI: 10.1063/5.0063301. [Online]. Available: <https://aip.scitation.org/doi/10.1063/5.0063301> (visited on 01/08/2022).
- [28] D. Winklehner, J. Conrad, J. Smolsky, *et al.*, “New Commissioning Results of the MIST-1 Multicusp Ion Source,” in *Journal of Physics: Conference Series*, vol. 2244, no. 1, p. 012013, Apr. 2022, Publisher: IOP Publishing, ISSN: 1742-6596. DOI: 10.1088/1742-6596/2244/1/012013. [Online]. Available: <https://doi.org/10.1088/1742-6596/2244/1/012013> (visited on 05/31/2022).
- [29] P. Weigel, M. Busza, A. Namazov, *et al.*, “The EPICS control system for IsoDAR,” *Nuclear Instruments and Methods in Physics Research Section A: Accelerators, Spectrometers, Detectors and Associated Equipment*, vol. 1056, p. 168590, Nov. 2023, ISSN: 0168-9002. DOI: 10.1016/j.nima.2023.168590. [Online]. Available: <https://www.sciencedirect.com/science/article/pii/S0168900223005806> (visited on 10/11/2023).

- [30] T. Kalvas, O. Tarvainen, T. Ropponen, *et al.*, “IBSIMU: A three-dimensional simulation software for charged particle optics,” *Review of Scientific Instruments*, vol. 81, no. 2, 02B703, Feb. 2010, Publisher: American Institute of Physics, ISSN: 0034-6748. DOI: 10.1063/1.3258608. [Online]. Available: <https://aip.scitation.org/doi/full/10.1063/1.3258608> (visited on 08/18/2020).
- [31] J.-L. Vay, D. P. Grote, R. H. Cohen, *et al.*, “Novel methods in the Particle-In-Cell accelerator Code-Framework Warp,” en, *Computational Science & Discovery*, vol. 5, no. 1, p. 014019, Dec. 2012, Publisher: IOP Publishing, ISSN: 1749-4699. DOI: 10.1088/1749-4699/5/1/014019. [Online]. Available: <https://dx.doi.org/10.1088/1749-4699/5/1/014019> (visited on 10/29/2023).
- [32] L. Waites, J. Conrad, J. Smolsky, *et al.*, “Matching of an RFQ and Multicusp Ion Source with Compact LEBT,” en, in *Proceedings of the 12th International Particle Accelerator Conference*, Artwork Size: 4 pages, 0.731 MB Medium: PDF, vol. IPAC2021, JACoW Publishing, Geneva, Switzerland, 2021, 4 pages, 0.731 MB, ISBN: 978-3-95450-214-1. DOI: 10.18429/JACOW-IPAC2021-MOPAB159. [Online]. Available: <https://jacow.org/ipac2021/doi/JACoW-IPAC2021-MOPAB159.html> (visited on 11/29/2021).
- [33] L. Waites, J. Conrad, and D. Winklehner, “A Low Energy Beam Transport to Match a Multicusp Ion Source to an RFQ,” en, *Journal of Physics: Conference Series*, vol. 2244, no. 1, p. 012086, Apr. 2022, Publisher: IOP Publishing, ISSN: 1742-6596. DOI: 10.1088/1742-6596/2244/1/012086. [Online]. Available: <https://doi.org/10.1088/1742-6596/2244/1/012086> (visited on 05/31/2022).
- [34] L. Waites, “High Power Cyclotrons: The Bridge Between Beyond the Standard Model Physics, Computation, and Medical Applications,” PhD, Massachusetts Institute of Technology, Cambridge, 2022. [Online]. Available: <https://arxiv.org/abs/2212.11114>.
- [35] U. Ratzinger, H. Podlech, M. Schütt, *et al.*, “Technical Design Report RFQ for IsoDAR,” English, Bevatech, GmbH, Technical Report, 2020, p. 60.
- [36] D. Winklehner, J. Conrad, D. Koser, *et al.*, “High-Current H₂⁺ Beams from a Compact Cyclotron using RFQ Direct Injection,” en, in *Proceedings of the 12th International Particle Accelerator Conference*, Artwork Size: 4 pages, 0.582 MB Medium: PDF, vol. IPAC2021, JACoW Publishing, Geneva, Switzerland, 2021, 4 pages, 0.582 MB, ISBN: 978-3-95450-214-1. DOI: 10.18429/JACOW-IPAC2021-TUXB07. [Online]. Available: <https://jacow.org/ipac2021/doi/JACoW-IPAC2021-TUXB07.html> (visited on 11/29/2021).
- [37] H. Höltermann, J. Conrad, D. Koser, *et al.*, “Technical Design of an RFQ Injector for the IsoDAR Cyclotron,” en, in *Proceedings of the 12th International Particle Accelerator Conference*, Artwork Size: 3 pages, 1.017 MB Medium: PDF, vol. IPAC2021, JACoW Publishing, Geneva, Switzerland, 2021, 3 pages, 1.017 MB, ISBN: 978-3-95450-214-1. DOI: 10.18429/JACOW-IPAC2021-THPAB167. [Online]. Available: <https://jacow.org/ipac2021/doi/JACoW-IPAC2021-THPAB167.html> (visited on 11/29/2021).
- [38] M. Sangroula, J. Conrad, M. Schuett, *et al.*, “Design and Optimization of a Low Frequency RF-Input Coupler for the IsoDAR RFQ,” en, in *Proceedings of the 12th International Particle Accelerator Conference*, Artwork Size: 4 pages, 0.877 MB Medium: PDF, vol. IPAC2021, JACoW Publishing, Geneva, Switzerland, 2021, 4 pages, 0.877 MB,

- ISBN: 978-3-95450-214-1. DOI: 10.18429/JACOW-IPAC2021-WEPAB195. [Online]. Available: <https://jacow.org/ipac2021/doi/JACoW-IPAC2021-WEPAB195.html> (visited on 10/11/2022).
- [39] D. Koser, J. Conrad, H. Podlech, *et al.*, “Thermal Analysis of a Compact Split-Coaxial CW RFQ for the IsoDAR RFQ-DIP,” en, in *Proceedings of the 12th International Particle Accelerator Conference*, Artwork Size: 3 pages, 12.334 MB Medium: PDF, vol. IPAC2021, JACoW Publishing, Geneva, Switzerland, 2021, 3 pages, 12.334 MB, ISBN: 978-3-95450-214-1. DOI: 10.18429/JACOW-IPAC2021-WEPAB202. [Online]. Available: <https://jacow.org/ipac2021/doi/JACoW-IPAC2021-WEPAB202.html> (visited on 11/29/2021).
 - [40] D. Koser, L. Waites, D. Winklehner, *et al.*, “Input Beam Matching and Beam Dynamics Design Optimizations of the IsoDAR RFQ Using Statistical and Machine Learning Techniques,” *Frontiers in Physics*, vol. 10, 2022, ISSN: 2296-424X. [Online]. Available: <https://www.frontiersin.org/article/10.3389/fphy.2022.875889> (visited on 04/25/2022).
 - [41] J. Alonso, S. Axani, L. Calabretta, *et al.*, “The IsoDAR high intensity H_2^+ transport and injection tests,” en, *Journal of Instrumentation*, vol. 10, no. 10, T10003, 2015, ISSN: 1748-0221. DOI: 10.1088/1748-0221/10/10/T10003. [Online]. Available: <http://stacks.iop.org/1748-0221/10/i=10/a=T10003> (visited on 10/16/2018).
 - [42] A. Adelmann, P. Calvo, M. Frey, *et al.*, *OPAL a Versatile Tool for Charged Particle Accelerator Simulations*, arXiv: 1905.06654, May 2019. [Online]. Available: <http://arxiv.org/abs/1905.06654> (visited on 10/10/2019).
 - [43] CST. “CST Microwave Studio - 3D EM Simulation Software.” (), [Online]. Available: <https://www.cst.com/Products/CSTMWS> (visited on 09/01/2015).
 - [44] *Cast iron specification by ion beam applications s.a., as provided to foundries*, Private Communication, 2023.
 - [45] Mouvers. “SPMT Voyager.” (2024), [Online]. Available: <https://www.mouvers.it/en/self-propelled-modular-transporter/> (visited on 02/21/2024).
 - [46] J. R. Alonso, K. M. Bang, R. Barlow, *et al.*, *IsoDAR@Yemilab: A Conceptual Design Report for the Deployment of the Isotope Decay-At-Rest Experiment in Korea’s New Underground Laboratory, Yemilab*, arXiv:2110.10635 [hep-ex, physics:physics], Dec. 2021. DOI: 10.48550/arXiv.2110.10635. [Online]. Available: <http://arxiv.org/abs/2110.10635> (visited on 02/23/2024).
 - [47] *The Present Status of TRIUMF*, vol. Proceedings of 1972 Cyclotron Conference, 1972.
 - [48] “GH Cranes.” (), [Online]. Available: <https://www.ghcranes.com/en/%7D> (visited on 02/22/2024).